Numerical vs experimental pressure drops for Boger fluids in sharp-corner contraction flow

J. E. López-Aguilar[a], H.R.Tamaddon-Jahromi[a], M.F. Webster[a] and K. Walters[b]

[a] Institute of Non-Newtonian Fluid Mechanics, Swansea University, College of Engineering, Bay Campus, Fabian Way, Swansea, SA1 8EN, UK

[b] Institute of Mathematics, Physics and Computer Science, University of Aberystwyth, Aberystwyth, SY23 3BZ, UK

Abstract

This paper addresses the problem of matching experimental findings with numerical prediction for the extreme experimental levels of pressure-drops observed in the 4:1 sharp-corner contraction flows, as reported by Nigen and Walters (2002). In this connection, we report on significant success in achieving *quantitative* agreement between predictions and experiments. This has been made possible by using a new swanINNFM model, employing an additional dissipative function. Notably, one can observe that extremely large pressure-drops may be attained with a suitable selection of the extensional viscous time-scale. In addition, and on vortex structure, the early and immediate vortex enhancement for Boger fluids in axisymmetric contractions has also been reproduced, which is shown to be absent in planar counterparts.

Keywords: Pressure-drops, Contraction flow, Vortex enhancement, swanINNFM model

1. Introduction

This study addresses the problem of matching experimental findings with numerical prediction for the extreme experimental levels of pressure-drops observed in some contraction flows observed by Nigen and Walters (2002). There, significant differences in response were observed between Boger and Newtonian fluids in steady-state *axisymmetric contraction* flow, which were not apparent in planar counterpart geometries. Here, the new swanINNFM model [Tamaddon-Jahromi *et al.* (2016)] is used, which has already proved capable of reproducing large experimental excess pressure-drops (*epd*) reported for contraction-expansion flow, within smooth corner geometries as in Rothstein and McKinley (2001). Importantly, contraction flow with sharp corners is a more severe problem to address, offering elevation in pressure-drops of one-order higher than for contraction-expansion flow. It is shown through the present predictive solutions how the new swanINNFM model, with its intrinsic dissipative-factor contributions, can deliver such high levels of experimental pressure-drops for *axisymmetric* contraction

flow, whilst also showing stress overshoots in transient flows. Alongside such findings with increasing flow-rate, the corresponding development of flow structure has also been investigated.

In the present paper, numerical computations have been performed through a finite element/finite volume (*fe/fv*) algorithm, which draws upon some recent and important advances in computational solution strategies to derive high deformation-rate viscoelastic steady-state solutions in complex flows. This includes using compatible stress/velocity-gradient representation on parent-subcell discretisation, ABS-f-functional constitutive correction (for structure functional f), and a strong centreline continuity/velocity-gradient enforcement. The *major conclusion* to be drawn from the current investigation is that, by using an appropriate constitutive model and a modern numerical technique, it is possible to obtain *quantitative* agreement between experiment and numerical prediction in an important rheological flow problem.

2. Background

In recent decades, there has been considerable activity in the fields of Experimental Rheology and Computational Non-Newtonian Fluid Mechanics. Much progress has been made on all fronts. So far as experiments are concerned, there have been major advances in a number of test problems, most notably contraction flows, flow past a sphere, splashing, and extrudate swell. However, there has often been a frustrating lack of agreement between experimental results and numerical predictions for Boger fluids, and particularly so, on enhanced pressure-drops in contraction-flows and drags in settling problems; see, for example, Tanner 2000, Walters and Webster, 2003; Phillips and Williams, 2002; Alves *et al*., 2004; Aboubacar *et al*., 2002; agreement has however been established on flow-structure, but not necessarily at comparable deformation rates). This is entirely so as regards continuum modelling, though mesoscopic approaches have begun to move in the right direction. So, for example, Castillo-Tejas *et al*. (2014) performed simulations on such Boger fluids, using *non-equilibrium molecular dynamics* and on abrupt contraction-expansion flows. Their molecular studies for circular contractions (aspect-ratio 4), predicted significant pressure-drop enhancement, the closest to experimental *epd*-findings of 300% being recorded as 150%. This certainly aids and points the way forward for continuum modelling. Whilst experimental data were being obtained and new numerical techniques were being developed, there was an understandable attitude of tolerance, with disagreements between theory and experiment being blamed on the constitutive models being employed, or deficiencies concerning the numerical techniques employed in what is a far more demanding research area than the corresponding Newtonian

Fluid Mechanics situation (see for example Boyd *et al.* 1984 and Owens and Phillips, 2002). Having said that, there has been a growing realization that the time has come to seek *quantitative* agreement between theoretical predictions and experimental results on pressure-drops particularly. Progress has already been made in some areas (see for example, Binding *et al* 2006; Walters et al 2009a, b; Pérez-Camacho *et al*. 2015; Garduño *et al*. 2016a, b; Tamaddon-Jahromi *et al*. 2016), and, in the present paper, we shall attempt to reach agreement in the important and demanding area of contraction flows with sharp corners. We shall consider both planar and axisymmetric configurations and, in particular, we shall attempt to interpret theoretically the provocative experimental results published by Nigen and Walters in 2002.

In our earlier work (see, for example, Walters et al. 2009a, b, Tamaddon-Jahromi *et al.* 2011, 2016), we attempted to make progress by considering a contraction/expansion geometry with rounded corners. In that geometry and context, it was possible to obtain reasonable (*qualitative*) agreement with the experimental results of Rothstein and McKinley (2001). However, we now feel that the time is ripe to seek (*quantitative*) agreement between theory and experiment on pressure-drops for the sharp-corner contraction–flow results of Nigen and Walters (2002), whilst covering both planar and axisymmetric contractions. Of course, the planar case does not present a significant problem, since viscoelasticity is expected to have a negligible effect on flow resistance in that case!

3. Governing equations and constitutive modelling

3.1 Viscoelastic flow modelling

Under an isothermal setting and for viscoelastic, incompressible flow, the relevant mass, conservation and momentum equations in non-dimensional forms are given by:

$$\nabla \cdot \boldsymbol{u} = 0, \tag{1}$$

$$Re\frac{\partial \boldsymbol{u}}{\partial t} = \nabla \cdot \boldsymbol{T} - Re\,\boldsymbol{u}\cdot\nabla\boldsymbol{u} - \nabla p, \tag{2}$$

$$\boldsymbol{T} = \boldsymbol{\tau}_p + \boldsymbol{\tau}_s, \tag{3}$$

where the field variables are $\boldsymbol{u}$ (fluid velocity), p (hydrodynamic pressure), $\boldsymbol{T}$ extra-stress, $\boldsymbol{\tau}_p$ (polymeric stress) and $\boldsymbol{\tau}_s$ (solvent stress). Here, $\boldsymbol{d}=(\nabla\boldsymbol{u}+\nabla\boldsymbol{u}^{\dagger})/2$ is the rate-of-deformation tensor (where superscript † denotes tensor transpose).

In addition, the non-dimensional group of the Reynolds number may be defined as $Re = (\rho U l / \mu_\circ)$, with characteristic scales of ρ for the fluid density, U for velocity, l for length (l/U for time), and a zero shear-rate viscosity $\mu_\circ = \mu_p + \mu_s$, for which μ_p is a polymeric viscosity and μ_s is a solvent viscosity. Then, the corresponding solvent-fraction becomes $\beta = \mu_s / \mu_\circ$. By default, the solvent contribution β is heavy and taken to be 0.9 (90%), which is compatible with the use of Boger fluids in the experiments. Here, creeping flow is assumed ($Re \approx O(10^{-2})$) and as a result, the momentum convection term contribution is negligible. Yet, since Re can be controlled through material properties (kinematic viscosity), this does not imply that Deborah numbers (De, see below for definition) are constrained to being low. There, either the strain-rate or relaxation-time can still be high in the Deborah number, as commonly encountered for Boger fluids. This permits the study of response under increasing elasticity through De alone, leading to high De and extensional viscosities at larger rates, which can generate significant elastic corner vortex growth.

Existing numerical studies for the Oldroyd B model have failed to predict the significant increases observed experimentally in the Couette correction (which is related to the pressure drop) for Boger fluids (see, for example, Aboubacar *et al*. 2002; Alves *et al*. 2003, Aguayo *et al*. 2008, Walters *et al*. 2008, 2009). Moreover, the lack of finite-extensibility of the Oldroyd-B model, and its over-strong quadratic response in the first normal stress difference N_1, are both features overcome in subsequent work, thereby drawing upon FENE-CR functionality (see Tamaddon-Jahromi *et al*. 2011).

As a consequence, a particular model variant, which we have called the swanINNFM(q) has been proposed, arising from the hybrid combination of well-respected White-Metzner and FENE-CR models (WM-FENE-CR, see developments in Tamaddon-Jahromi *et al.* 2011, 2016, and Garduño *et al*. 2016b). Such a model displays the desired properties of constant shear viscosity, finite extensibility (with a bounded extensional viscosity reaching an ultimate plateau), and a first-normal stress-difference ultimately weaker than quadratic. In configuration tensor form, with configuration tensor ($\mathbf{A}$), the swanINNFM(q) constitutive equation for this hybrid model may be expressed as:

$$\boldsymbol{T} = \boldsymbol{\tau}_p + \boldsymbol{\tau}_s = \frac{(1-\beta)}{De} \mathrm{f}(\mathrm{Tr}(\mathbf{A}))\mathbf{A}\phi(\dot{\varepsilon}) + 2\beta\phi(\dot{\varepsilon})\boldsymbol{d}\,, \tag{4}$$

$$De\,\overset{\nabla}{\mathbf{A}} + \mathrm{f}(\mathrm{Tr}(\mathrm{A}))(\mathrm{A} - \mathbf{I}) = \mathbf{0}\,, \tag{5}$$

where $\overset{\nabla}{\mathbf{A}}$ represents the upper-convected material derivative of $\mathbf{A}$ defined as:

$$\overset{\nabla}{\mathbf{A}} = \frac{\partial \mathrm{A}}{\partial t} + \mathbf{u}\cdot\nabla\mathbf{A} - (\nabla\mathbf{u})^{\dagger}\cdot\mathbf{A} - \mathbf{A}\cdot(\nabla\mathbf{u})\,. \tag{6}$$

The dissipative function $\phi(\dot{\varepsilon})$ is defined as $\phi(\dot{\varepsilon})=1+(\lambda_D\dot{\varepsilon})^2$, a truncated form of the cosh function (see Debbaut and Crochet 1988, Debbaut *et al*. 1988, Tamaddon-Jahromi *et al*. 2016, Garduño *et al*. 2016b), where λ_D is a material time constant and $\dot{\varepsilon}$ is a strain-rate. Following standard convention, a generalised strain-rate $\dot{\varepsilon}$ is that adopted based on the second and third invariants of the rate-of-deformation tensor $\boldsymbol{d}$, viz,

$$\dot{\varepsilon}=3\mathrm{III}_{\boldsymbol{d}}/\mathrm{II}_{\boldsymbol{d}}, \qquad (7)$$

where $\mathrm{II}_d=\frac{1}{2}\mathrm{tr}\left(\boldsymbol{d}^2\right)$, $\mathrm{III}_{\boldsymbol{d}}=det\left(\boldsymbol{d}\right)$.

In Eq.(7), $\dot{\varepsilon}$ is a generalised rate-of-strain for complex flow, based on the commonly used invariant form, that of the third invariant divided by the second invariant of the rate-of-deformation tensor[1] (definition-I; for discussion on choice, see for example, Debbaut and Crochet (1988)). Clearly, this generalised invariant form of $\dot{\varepsilon}$ has the correct scale and reduces to the usual extensional strain rate in a uniaxial extensional flow (as in Figure 1, see below). One notes the collapse of this model (Eqs. 4 and 5) into a FENE-CR base-form when $\phi(\dot{\varepsilon})=1$, as in pure shear flow, planar flow (via $\dot{\varepsilon}=0$; see also Appendix-II), or when $\lambda_D=0$. In the above, the FENE stretch function $\mathrm{f}(\mathrm{Tr}(\mathbf{A}))$ in (4) and (5) depends on the extensibility parameter L, and is given by:

$$f(\mathrm{Tr}(\mathbf{A}))=\frac{1}{1-\mathrm{Tr}(|\mathbf{A}|)/\mathrm{L}^2}. \qquad (8)$$

Then, an increasing value of *L*, results in a larger plateau-level of extensional viscosity.

One may provide an explanation *for the physical basis and understanding of the dissipative material time-scale parameter (λ_D)*, which substantiates the strong *extensional* dissipative response. So, for example, fibre suspension additives would point the way here to such a physical mechanism, providing dissipative extensional behaviour, and hence strong strain-hardening effects (yet with little impact on shear properties, see Abdul-Karem et al. (1993) and Baloch and Webster (1995). Since this idea may be applied under scale-reduction, at the mesoscopic-level to the molecular-level, one can well see how appropriate physics may be constructed to substantiate such effects. One must emphasize at this point, that the swanINNFM(q) model, with an extension-rate dependent viscosity (constant in shear), has already proven well capable of capturing the levels of enhanced pressure drop (Tamaddon-Jahromi *et al.* 2016) (and drag in counterpart settling flows (Garduño *et al.* 2016b), observed in experimental

[1] Or, for regularisation in regions of vanishing $\mathrm{II}_{\boldsymbol{d}}$, division by $(1+\mathrm{II}_{\boldsymbol{d}})$. This would occur on the centreline in shear-free flow.

measurements, over a wide range of flow rates. To the author's knowledge, proved possible with *any other continuum-based* model. The present modelling work attempts to distinguish differences associated with and boost extensional viscosity behaviour (hardening), by introducing extensional dissipative effects (inactive in shear) through the incorporation of λ_D and dissipative stress, with its impact on pressure-drops (see also arguments in Rothstein & McKinley 1999 on this point). Moreover, experience would dictate that, it is often found difficult to derive a good parameter match and fitting to both experimental shear and elongational data, simultaneously. One notes the experimental *epd*-data does not come with a prescribed extensional viscosity (yet to be determined); hence from a predictive viewpoint, one only has the pressure-drop data to work with.

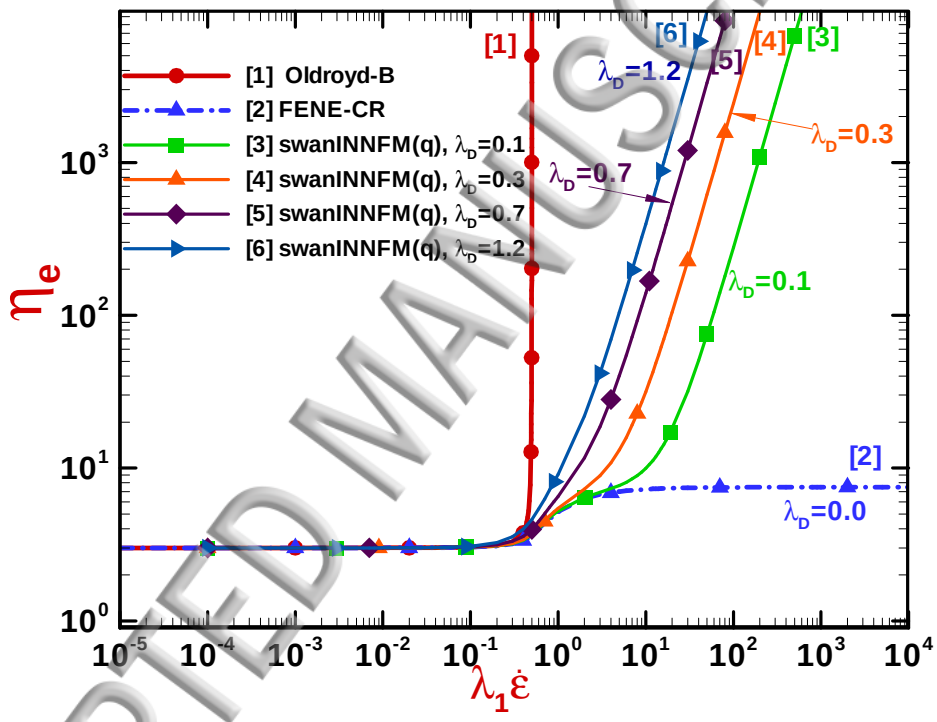

Figure 1 Extensional viscosity for Oldroyd-B, FENE-CR, and swanINNFM(q) models, λ_D=[0.0, 1.2]

swanINNFM(q) extensional viscosity

The extensional viscosity (η_e) for the swanINNFM(q) model is plotted in Figure 1 against the product of extensional strain rate ($\dot{\varepsilon}$), and a single-averaged relaxation time (λ_1). Then, the data covers a range of dissipative factors, $0 \leq \lambda_D \leq 1.2$. Recognising that this model only departs from the conventional rheological response of the FENE-CR model (λ_D=0) in extensional deformation, such data is plotted

against equivalent forms for FENE-CR and Oldroyd-B models. Here, a rising trend in extensional viscosity is clearly observed for swanINNFM(q) (λ_D >0, strain-rates>0.5), when compared to the FENE-CR(λ_D =0) base-model form; yet this is considerably less than that attributable to an Oldroyd-B response for strain-rates 0.5 units and above. Notably, the (λ_D =0.1)-curve captures the FENE-CR(λ_D =0) base-model form up to its second limiting-plateau at high rates; departing in response around strain-rates of O(3) units, rising sharply thereafter. With elevation to λ_D =0.3 and λ_D =0.7, such departure occurs earlier at ~1.5 and ~ 0.7 strain-rate units, respectively. In contrast, for a considerably larger λ_D of 1.2, the departure has shifted to ~0.3 strain-rates units, over a decade earlier. Then, the associated rheometrical functions for the swanINNFM(q) model are those for model parameters, β =0.9, L=5 and $0 \leq \lambda_D \leq 1.2$; which can be represented as:

$$\eta = \eta_0,$$
$$\mathrm{N}_1^{shear} = \frac{2\eta_0(1-\beta)De\dot{\gamma}^2}{f}, \quad \mathrm{N}_2^{shear} = 0, \tag{9}$$
$$\eta_e = 3\phi(\dot{\varepsilon})\beta\eta_0 + 3\phi(\dot{\varepsilon})(1-\beta)\eta_0\left[\frac{f^2}{f^2 - f\,De\dot{\varepsilon} - 2De^2\dot{\varepsilon}^2}\right],$$

where $\dot{\gamma} = 2\sqrt{\mathrm{II}_{\boldsymbol{d}}}$ is a shear-rate based on the second invariant of the rate-of-deformation tensor $\boldsymbol{d}$, and $f = f(Tr(\mathbf{A}))$, as above.

4. Numerical method and discretisation

4.1 Hybrid finite element/finite volume scheme

The particular form of the hybrid parent finite element/subcell finite volume method (*fe/fv*) has been much reported elsewhere, (see Webster et al. 2005; Matallah *et al.* 1998). In essence, this employs a semi-implicit, time-splitting, fractional-staged formulation, which invokes finite element discretisation (on the parent cell) for velocity-pressure parts of the system, and finite volume for stress (on child subcells). The time-stepping is cast about a Taylor–Galerkin (TG) discretisation, relying upon a two-step Lax-Wendroff time stepping procedure (predictor-corrector), grafted upon an *incremental pressure-correction* (*i*PC) procedure. Such a pressure-correction implementation ensures second-order temporal accuracy under incompressibility conditions. Utilising concise semi-discrete time-discretisation, as described in Wapperom and Webster (1998), Webster *et al.* (2005) and Belblidia *et al.* (2008), the schematic representation of the combined three-stage TGPC structure may be expressed on a single time

step $\Delta t=[t^n, t^{n+1}]$ with initial values $[u^0; v^0, p^0, p^{-1}]$. Typical time-steps employed are of the order $O(10^{-4})$ and a relative-increment time-stepping termination tolerance is selected (by default) of the order of 10^{-6} to determine temporal convergence to a steady state.

In summary, a Galerkin discretisation may be applied to the Navier-Stokesian components of the system; with the momentum equation at Stage 1, the pressure-correction step at Stage 2, and incompressible correction constraint at Stage 3. To enhance stability, the diffusion term is treated in a semi-implicit manner. This avoids the computational overhead of a fully-implicit alternative. Pressure temporal increments invoke multi-step reference to three successive time levels $[t^{n-1}, t^n, t^{n+1}]$ across the various fractional-stepped equations.

Once spatial discretisation has been conducted, *strain-rate stabilisation* (SRS-term) may be enforced, via a deferred-correction difference-factor term D-D_c. This technique has been well documented elsewhere, with its basis lying in *fe*-GLS formalization; (see Guènette and Fortin (1995); Baaijens (1998); and Walters and Webster (2003)). The weighted-residual form of the *strain-rate stabilisation* difference-factor term D-D_c is

$$\int_\Omega \varphi_i 2\hat{\alpha}\mu_s \nabla\cdot(\boldsymbol{d}-\boldsymbol{d}_c)^n d\Omega, \qquad (10)$$

with respect to domain Ω and weighting function $\varphi_i(x)$. In this expression, $\hat{\alpha}$ is a stabilisation parameter, $\boldsymbol{d}$ the *fe*-discontinuous rate of deformation tensor, and $\boldsymbol{d}_c$ its continuous and recovered equivalent, based on a localized velocity-gradient recovery procedure (Belblidia *et al*. 2008).

Further to the above, two additional and recent techniques are utilised, termed ABS-f-correction and VGR-correction. These procedures have been introduced elsewhere in López-Aguilar *et al.* (2015), in the context of thixotropic modelling, and in Tamaddon-Jahromi *et al.* (2016), whilst modelling Boger fluids in contraction-expansion flow. The ABS-f-correction avoids the possibility of the dissipation function in the constitutive equation becoming negative, thus predicting negative values of the viscosity and structure f-functional during flow evolution. The VGR-correction refers to the particular velocity-gradient recovery-correction procedure applied, with its strong centreline continuity enforcement through velocity-gradient imposition, which prevents build-up of spurious numerical noise in solution evolution.

4.2 Finite-volume cell-vertex discretisation for configuration tensor

Nodal stress values are computed at the vertices of each *fv*-subcell. Cell-vertex finite volume techniques in the viscoelastic context have been presented in detail elsewhere (Matallah *et al*. 1998,

Belblidia *et al.* 2018). Hence only a brief description of the underlying theory is provided, as may be gathered from the non-conservative configuration-tensor form equation, through time derivative ($\frac{\partial \boldsymbol{A}}{\partial t}$), flux ($\boldsymbol{R} = \boldsymbol{u} \cdot \nabla \boldsymbol{A},$) and source ($\boldsymbol{Q}$) terms. Then, cell-vertex *fv*-schemes are applied to this differential equation utilising fluctuation distribution (as the upwinding technique of choice), to distribute control volume residuals and furnish nodal solution updates (Wapperom and Webster 1998). We consider each scalar configuration tensor component, $\mathbf{A}$, to act on an arbitrary volume $\Omega = \sum_l \Omega_l$, whose variation is controlled through the corresponding fluctuation components of flux ($\boldsymbol{R}$) and source ($\boldsymbol{Q}$). Then

$$\frac{\partial}{\partial t}\int_{\Omega_l} \mathbf{A} d\Omega = -\int_{\Omega_l} \boldsymbol{R} d\Omega + \int_{\Omega_l} \boldsymbol{Q} d\Omega \,. \tag{11}$$

Such integral flux and source variations are evaluated over each finite volume triangle (Ω_l), and are allocated proportionally by the selected cell-vertex distribution (upwinding) scheme to its three vertices. The nodal update is obtained by summing all contributions from its control volume Ω_l, composed of all *fv*-triangles surrounding node (l). In addition, these flux and source residuals may be evaluated over two separate control volumes, each associated with a given node (l) within the *fv*-cell T. This procedure generates two contributions: the first contribution is upwinded and governed over the *fv-triangle T*, ($\boldsymbol{R}_T$, $\boldsymbol{Q}_T$); the second contribution is area-averaged and subtended over its unique *median-dual-cell* zone, ($\boldsymbol{R}_{mdc}$, $\boldsymbol{Q}_{mdc}$).

In this manner, a generalized *fv*-nodal update equation has been derived, per the configuration-tensor component (Webster *et al.* 2005), incorporating appropriate area-weighting to maintain temporal consistency. This has led to a separate treatment of individual time derivative, flux and source terms. Once integrated over associated control volumes, the corresponding *fv*-nodal update stencil becomes

$$\left[\sum_{\forall T_l} \delta_T \alpha_i^T \Omega_T + \sum_{\forall mdc_l} (1-\delta_T)\hat{\Omega}_l^T\right] \frac{\Delta \mathbf{A}_l^{n+1}}{\Delta t} = \sum_{\forall T_l} \delta_T \alpha_i^T \boldsymbol{b}^T + \sum_{\forall mdc_l} (1-\delta_T)\boldsymbol{b}_l^{mdc} \,, \tag{12}$$

where $\boldsymbol{b}^T = (-\boldsymbol{R}_T + \boldsymbol{Q}_T)$, $\boldsymbol{b}_l^{mdc} = (-\boldsymbol{R}_{mdc} + \boldsymbol{Q}_{mdc})^l$, Ω_T is the area of the *fv*-triangle T, and $\hat{\Omega}_l^T$ is the area of its median-dual-cell (*mdc*). Here, the weighting parameter $0 \le \delta_T \le 1$ proportions the balance taken between contributions from the *median-dual-cell* and the *fv-triangle* T. The background detail and notation follow Wapperom and Webster (1998), illustrating such detailed aspects as: the interconnectivity of the selected set of *fv*-triangular cells (T_l) surrounding the sample node (l); their subtended set of median-dual-cell *(mdc_l)* zones (each within a cell (T_l) and linked with sample node (l));

the associated containing set of parameters, and the flow-kinematics distribution. (*fv*-upwinding) parameters (α_i^T), for *i = 1,2,3* on each *fv*-cell ($T = T_l$).

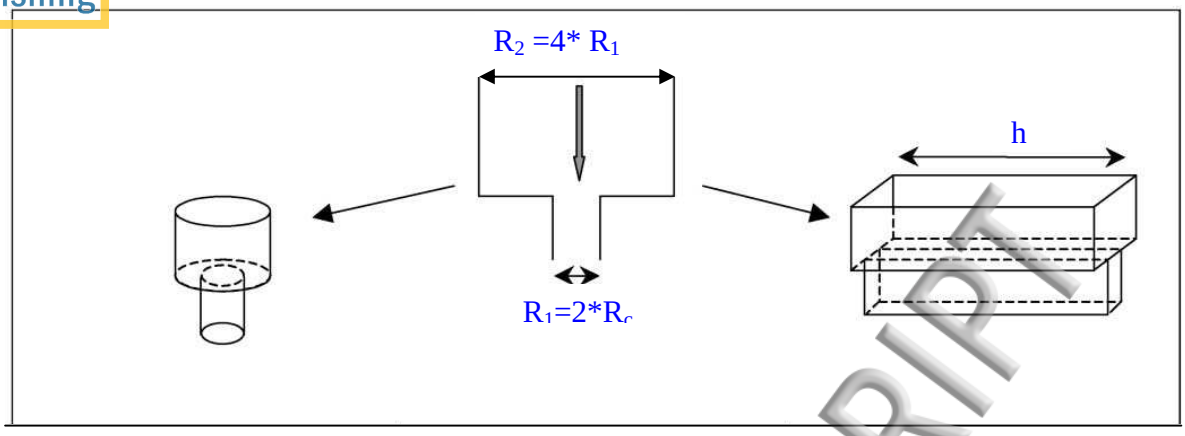

Figure 2. Schematic diagrams, flow through 4:1 planar and axisymmetric contractions

5. Problem specification

A schematic presentation of the flow geometries is provided in Figure 2, both planar and circular-symmetric (axisymmetric), reflecting the relevant 4:1 ratio, sharp-corner configuration (and definitions of length parameters, R_c, R_1, R_2, h). Figure 3 displays the triangular structure, refinement zones and meshing chosen (with characteristic numbers of elements, nodes, degrees-of-freedom (dof), and minimum-element size (h-min)). This choice illustrates the zoomed section around the re-entrant corner, where refinement is based on mesh density in the contraction region. In addition, two summary matrix-tables of the current situation and findings for axisymmetric/planar contractions are provided by the current authors in Table 1 (experimental observations) and Table 2 (numerical predictions) for both shear-thinning and constant-viscosity (Boger) fluids. These data provide a time-dated snap-shot of expectation on vortex enhancement and increased pressure-drops, with justification for the various entries in these tables being provided in Boger and Walters (1993); Boger *et al*. (1986); Walters and Rawlinson (1982); Walters and Tanner (1992) and elsewhere. So, we show in Table 2 the computational matrix corresponding to Table 1. Here and in terms of calibrating vortex enhancement, we particularly report on change in vortex intensity/strength in the predictions below. We also record counterpart upstream vortex length, but note that changes in this metric are much reduced, as overall vortex-size does not tend to alter anything like as much as intensity.

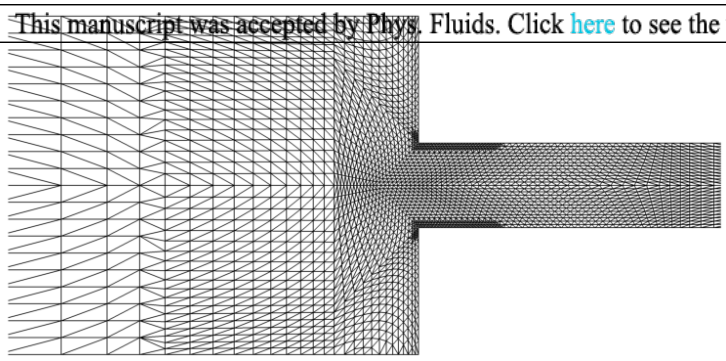

Figure 3. Zoomed mesh sections, 4:1 contraction geometry (*elements=2986, nodes=6220, dof=38937, h-min=0.0063*)

Table 1. Experimental observations, (e.g. Nigen and Walters 2002)

	Planar		Axisymmetric	
	Vortex enhancement	Increased pressure drop	Vortex enhancement	Increased pressure drop
Constant-viscosity Boger fluids	No	No	Yes	Yes!
Shear-thinning polymer solutions	Yes	Yes	Yes	Yes

Table 2. Numerical predictions, (e.g. Binding *et al.* 2006, Tamaddon-Jahromi *et al.* 2011)

	Planar		Axisymmetric	
	Vortex enhancement	Increased pressure drop	Vortex enhancement	Increased pressure drop
Constant-viscosity Boger fluids	No	No	Yes	No
Shear-thinning polymer solutions	Yes	Yes	Yes	Yes

Our preoccupation in the present paper is to interpret the Nigen and Walters (2002) experiments for Boger fluids (Boger 1977/78). Specifically, we wish to interpret the provocative experimental data provided in Figure 4 for a Boger fluid in axisymmetric 4:1 contractions. Note that, with the fluid density of $\rho \sim 1.4$ mg/mm^3 (Nigen and Walters, 2002) in Figure 4, the pressure-drop (ΔP) and flow-rate (Q) are scaled, respectively, by $\Delta P_0 = 10^5$ Pa and $Q_0 = Q_0 \left(\frac{1.5 g/s}{0.0014 g/mm^3} \right)$. The corresponding experimental measurements for the 4:1 planar contraction are shown in Figure 5, where pressure-drop and flow-rate are again scaled with ($\Delta P_0 = (4.464 * 10^9)$Pa), and [$Q_0 = Q_0 \left(1 mm^3/s\right)$].

Typical forms of Group Deborah number employed in the cited references are: in the experiments, (e.g. *axisymmetric*, $De_{\lambda_1}^{Exp} = \lambda_1^{Exp} \frac{Q}{\pi R_c^3}$, $\lambda_1^{Exp} = 0.16s$); and in the simulations ($De_{\lambda_1}^{Sim} = \lambda_1^{Sim} \bar{U}/\bar{L}$). Recognising that the *modus operandum* here is to vary deformation rate (from a base unit-reference, increasing flow-rate), hence a single common Deborah number may be established through the ratio between experimental and simulation *relaxation-times* (each taken as a single-averaged estimate). So, for example, in the present circular context, this identifies a relational scaling factor of 10, which yields: $De_{\lambda_1}^{Exp} = 10 De_{\lambda_1}^{Sim}$. Furthermore, under the *planar setting*, the experimental Deborah number is given by: $De_{\lambda_1}^{Exp} = \lambda_1 \dot{\gamma} = \lambda_1 \frac{Q}{hR_1^2/2} = \lambda_1 \frac{2Q}{hR_1^2}$, where $\dot{\gamma}$ is a mean shear-rate in the constriction-gap of the contraction, R_1 is the width of the contraction, and h is the height of the channel (in the third dimension). This implies that the cross-sectional area of the constriction-gap is ($A_c = hR_1$), over which the flow-rate (Q) is determined, with a characteristic length taken as the half-gap-width ($\bar{L} = R_1/2 = R_c$). Then, $\dot{\gamma} = \frac{Q}{A_c(R_1/2)} = \bar{U}/\bar{L}$. In the planar context, an equivalent relational scaling factor of 3.3 emerges, where: $De_{\lambda_1}^{Exp} \approx 3.3 De_{\lambda_1}^{Sim}$.

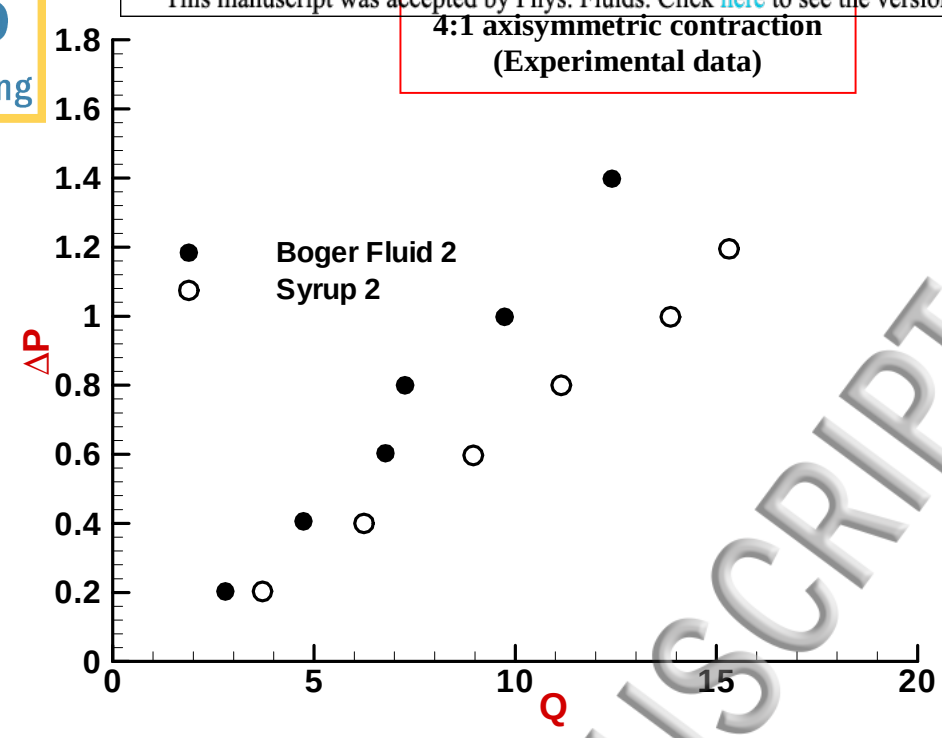

Figure 4. Pressure/flow-rate data (scaled), Nigen and Walters (2002), 4:1 *axisymmetric contraction*

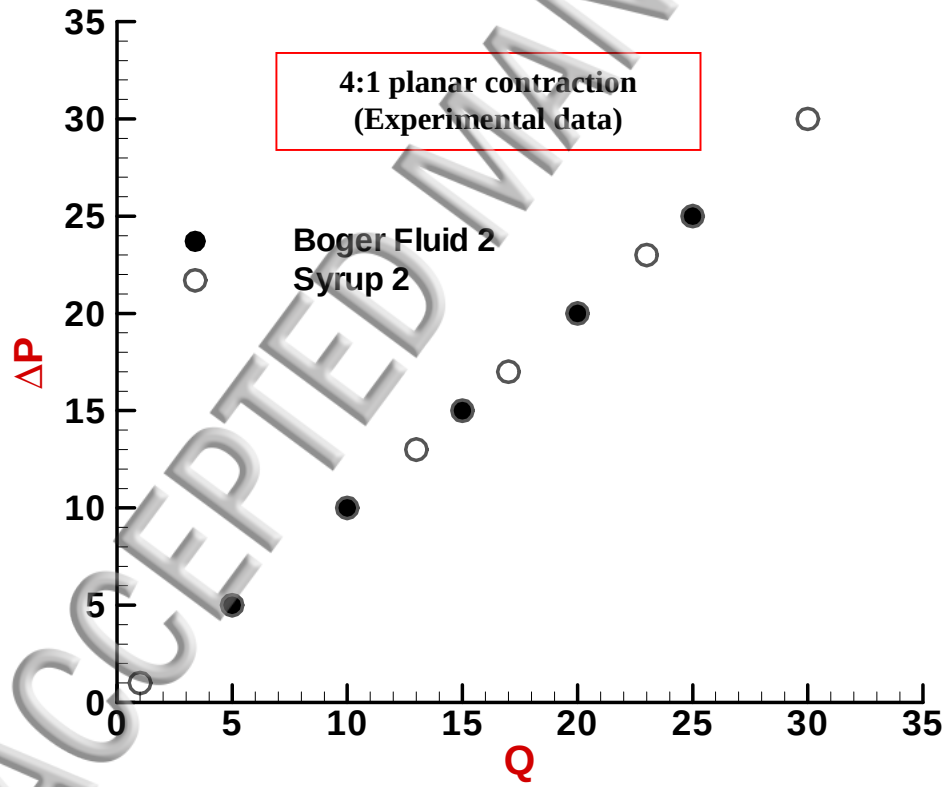

Figure 5. Pressure/flow-rate data (scaled), Nigen and Walters (2002), 4:1 *planar contraction*

6. Numerical Predictions

6.1 Circular case

Effect of constitutive equation parameter (*variation in dissipative factor,* λ_D)

The influence of the dissipative material time-scale parameter (λ_D) on the total pressure-drop is shown in Figure 6a, with solvent viscosity β=0.9. High values of the λ_D factor correspond to higher extensional viscosity at ranges beyond $\lambda_1\dot{\varepsilon}>0.5$ (see Figure 1). The effect of λ_D on pressure-drop at flow rates of Q<4 units are insignificant, whilst, for higher flow-rates, larger pressure-drops are clearly visible as λ_D increases. For example, a change from λ_D=0.3 to λ_D=1.2, at fixed Q=12 units, produce a pressure-drop of around 5400 units for λ_D=0.3 and 7350 units for λ_D=1.2 (~36% increase). Furthermore, in Figure 6b, the total pressure-drop is provided in comparative form for $0\leq\lambda_D\leq1.2$, the data spanning three different levels of flow-rate of Q=2.8, 7.2 and 12 units. Here, with increasing λ_D, there is no significant adjustment in pressure-drop observed at low flow-rate, Q=2.8 units. However, as flow-rate rises and for the higher value of Q=12 units, it is clearly apparent that increase in λ_D causes considerable elevation in pressure-drop.

One may consider the impact on vortex enhancement of an elevation in λ_D, in switching between λ_D=0.0 to λ_D=1.2 for different levels of flow-rate of Q=2.8, 7,2, and 12 units. As such, and at Q=12 units, salient-corner vortex-intensity rises to around ~220% from λ_D=0.3 (ψ_{min}=-0.954 units) to λ_D=1.2 (ψ_{min}=-3.08 units). For the corresponding λ_D-range at Q=7.2 units, vortex-intensity rises to ~44%, see Figures 7A, 7B. Then, such vortex enhancement can be associated with the counterpart generation of larger extensional viscosity, arising as it does from the increased dissipative factor, λ_D , for $\lambda_1\dot{\varepsilon}>0.5$ units.

It is also interesting to analyse in Figure 8 the impact of variation in dissipative factor (λ_D) at *fixed flow-rate*, taken here at the largest setting (Q=12 units). The position is interpreted through two trend graphs covering response in pressure-drop and vortex intensity. One notes that vanishing λ_D implies collapse of the swanINNFM(q) to that of the base FENE-CR form. Then for $0\leq\lambda_D\leq1.2$, one observes enhancement in vortex intensity from ~0.4 (λ_D=0) to ~3.2 (λ_D=1.2), with a counterpart rise in pressure-drops from 1.0 to ~1.4 (scaled by the representative pressure value at λ_D=0). Clearly, such rising trends are mutually linked.

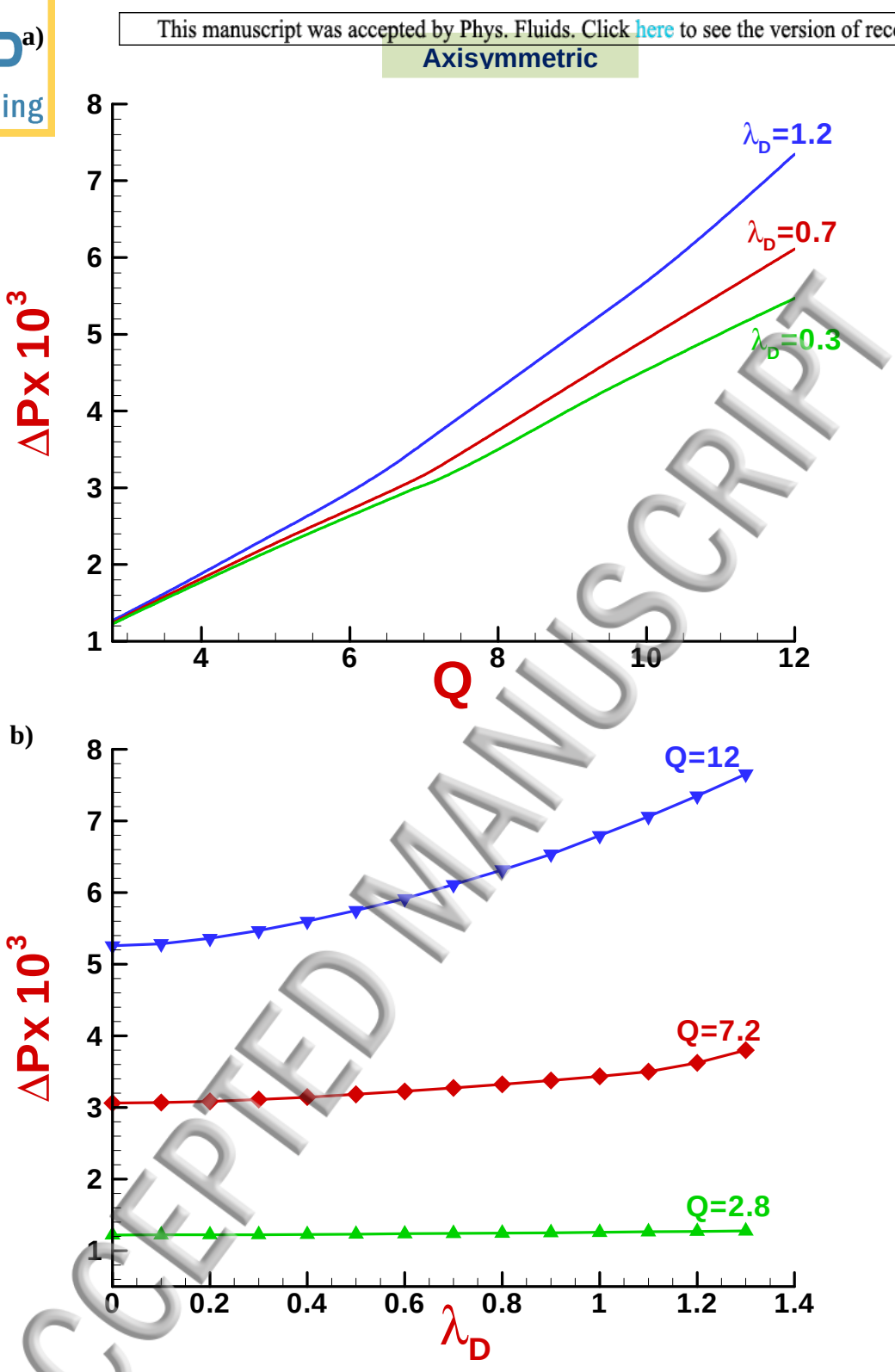

Figure 6. Pressure drop (ΔP), swanINNFM(q) model, Q=2.8, 7.2, 12; various λ_D, *axisymmetric contraction*

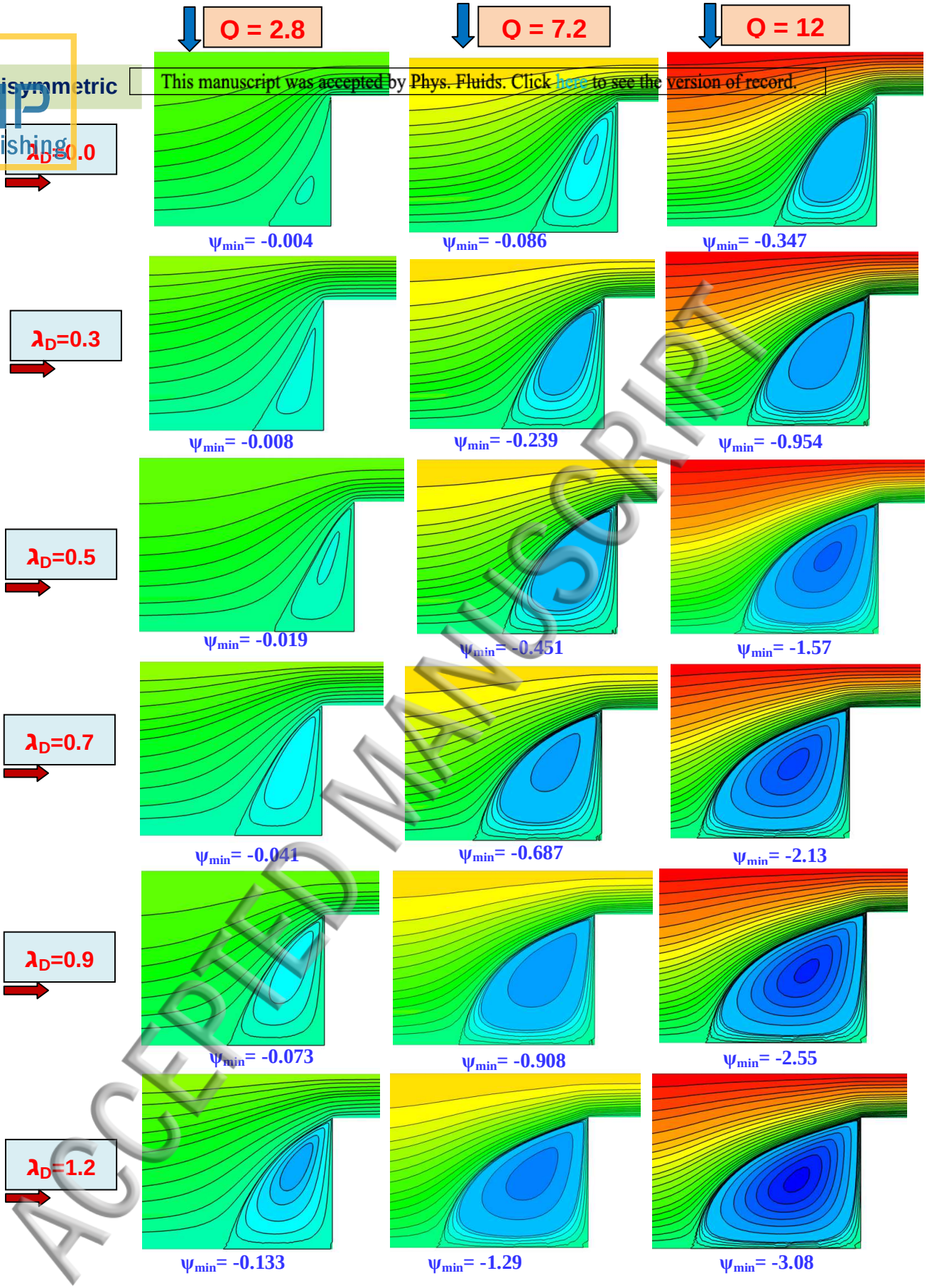

Figure 7A. Streamlines, swanINNFM(q) model, Q=2.8, 7.2, 12; λ_D=[0.0, 1.2], *axisymmetric contraction*

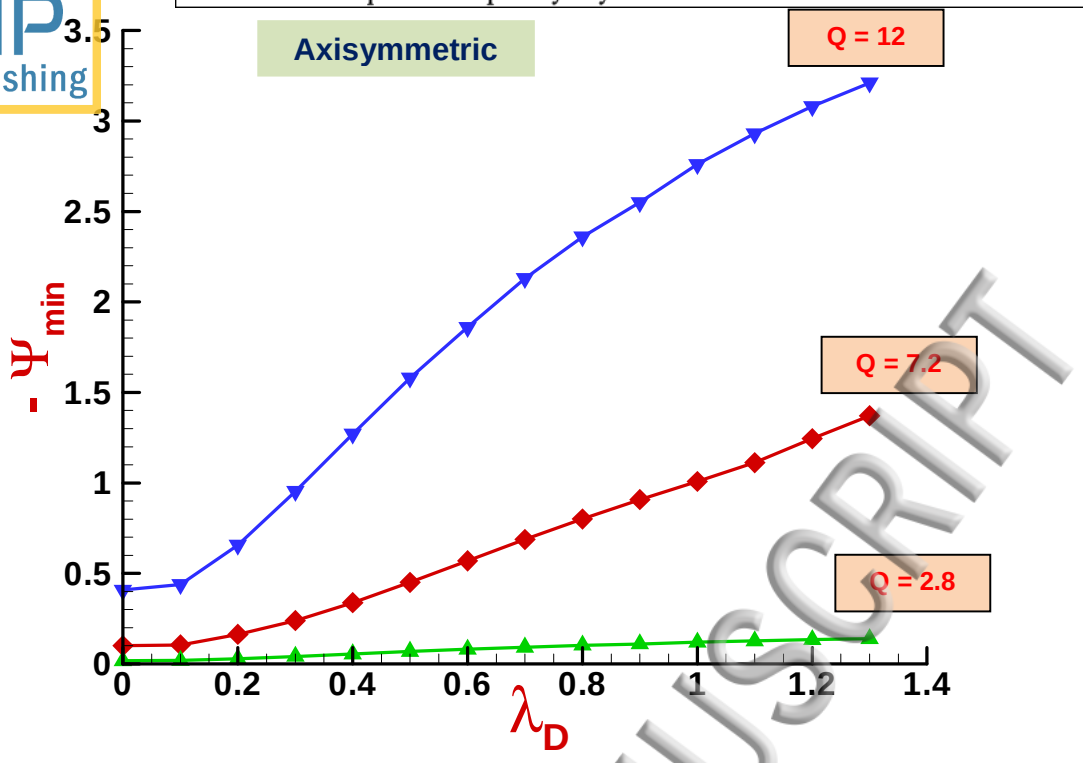

Figure 7B Salient corner vortex intensity (ψ_{min}), swanINNFM(q) model, Q=2.8, 7.2, 12; various λ_D, *axisymmetric contraction*

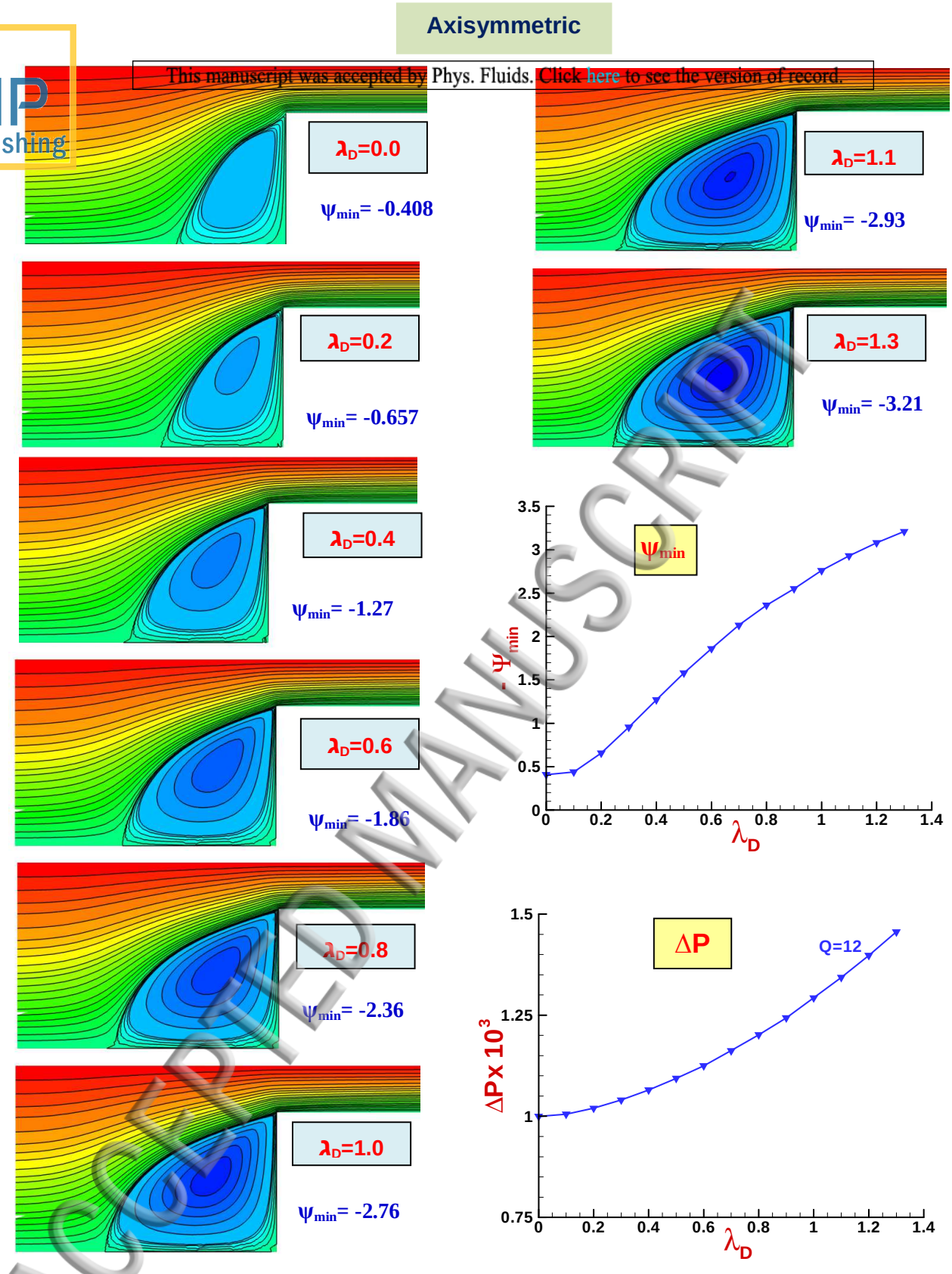

Figure 8. Streamlines, salient-corner vortex intensity (ψ_{min}), pressure drop (ΔP), swanINNFM(q) model, Q=12; various λ_D, *axisymmetric contraction*

Numerical predictions versus experimental data

The predictive matching for the 4:1 *axisymmetric* contraction data of Nigen and Walters (2002), covering pressure-drop (ΔP-scaled) versus flow-rate (Q-scaled) increase, is provided in summary in Figure 9. This conveys the sense that both the Newtonian position, with linear rise in the trend curve, and non-linear P-enhancement for the Boger Fluid 2 are quantitatively captured. Here, the swanINNFM(q, λ_D=1.2) has been used, with dissipative extensional-viscous time-scale factor of λ_D=1.2 to match the Boger Fluid data, which covers a significant range of flow-rates. The extensional response for this selection can be gathered from Figure1.

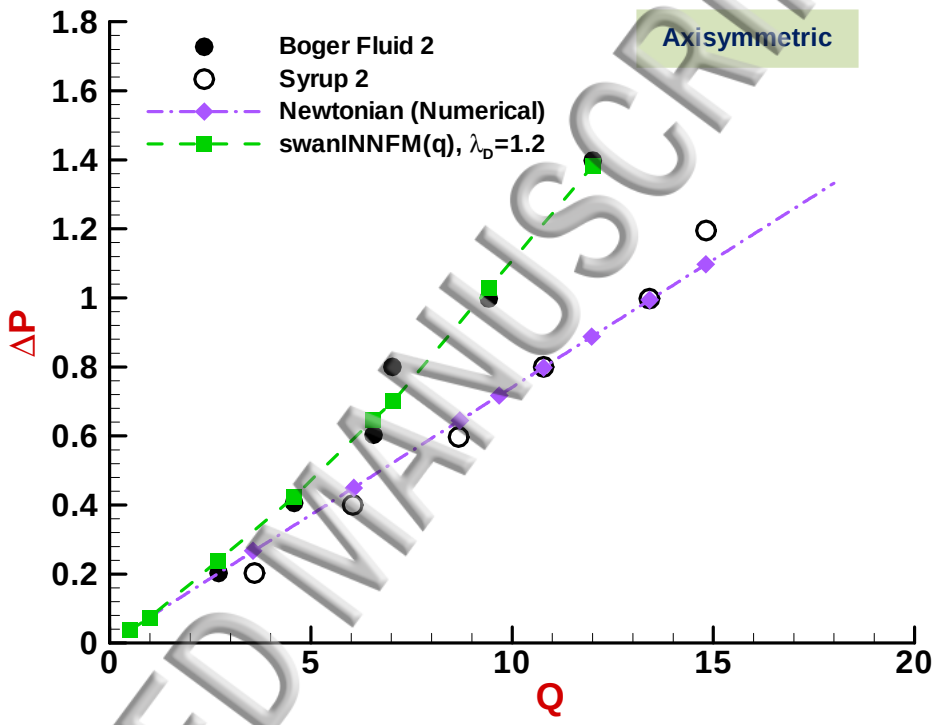

Figure 9. Pressure-drop vs flow-rate, Nigen and Walters (2002) 4:1 experimental vs swanINNFM(q, λ_D=1.2) model, *axisymmetric* contraction

The corresponding vortex enhancement trends with rising flow-rate are charted in Figure 10. This would indicate that there is indeed significant vortex growth as Q rises from ~2 to ~12 units. Here, a large recirculation region is present at flow-rates Q>6 units, occupying the whole region, from salient to re-entrant corner. This trend is amplified with rise in flow-rate to Q=12 units. Here, salient-corner vortex-intensity increases some twenty-three-times, from Q=2.8 to Q=12 units, and the separation streamline displays convex shape (from a recess corner perspective). Moreover, in Figure 10 when taken against increasing flow-rate, evolution is clearly apparent in the dimensionless salient-corner *upstream vortex-size* (L_U). In this data, the vortex-size for Q=12 units is some 1.5 times larger than that at Q=2.8

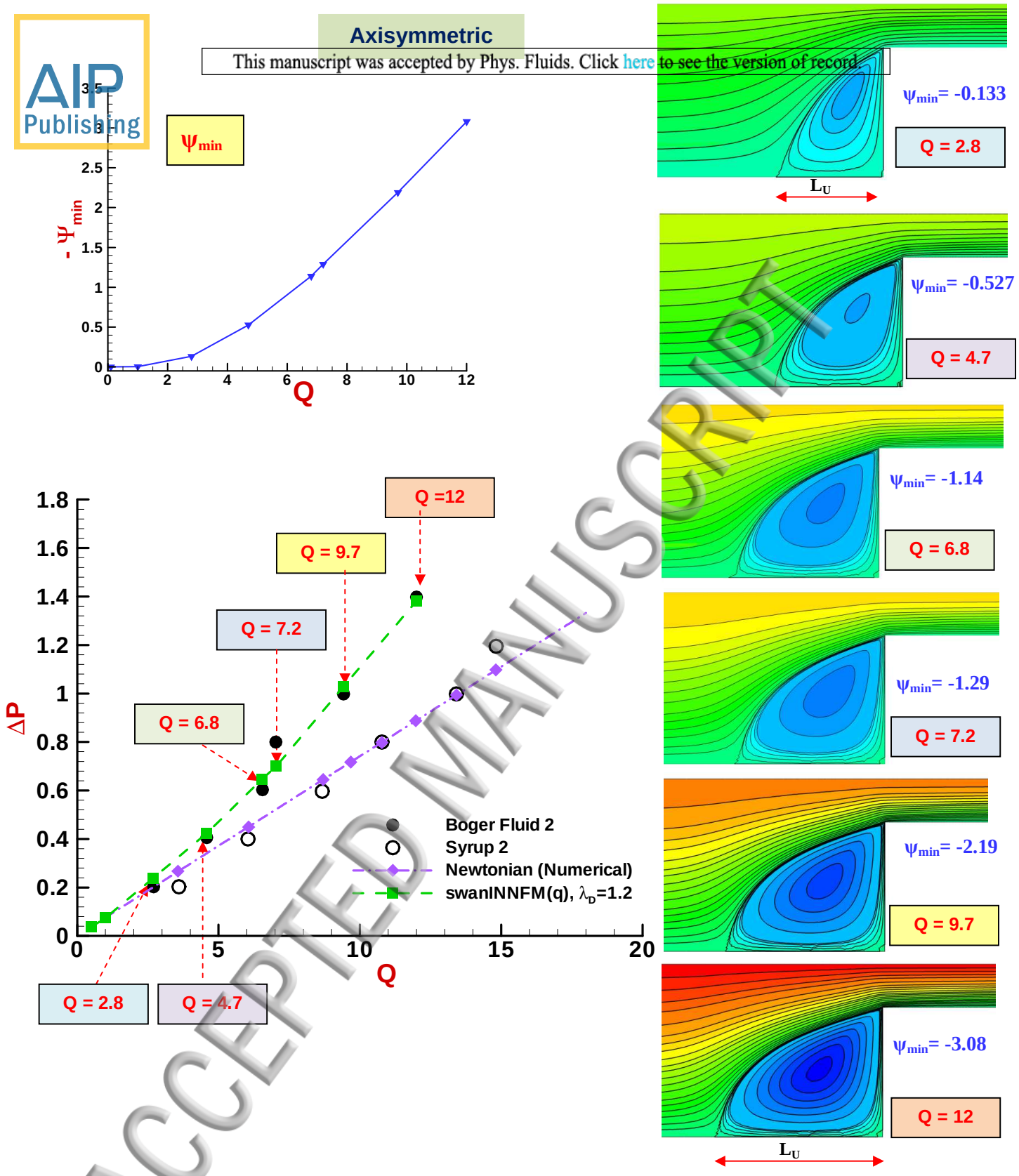

Figure 10. Pressure-drop vs flow-rate with corresponding streamlines, swanINNFM(q) model; λ_D=1.2, 4:1 *axisymmetric contraction*

units. The associated total pressure-drop in Boger fluids 0.24 units at Q=2.8 units, to 1.36 units at Q=12 units, representing a factor-increase of around 5.7. Such consistent correlation in flow response, corresponds to the strong initial strain-hardening (see Figure 1, in the range just beyond $\lambda_1\dot{\varepsilon}>0.5$). In itself, this observation confirms the proposition that extensional viscosity has a major role to play in enhancement of both pressure-drop and vortex activity.

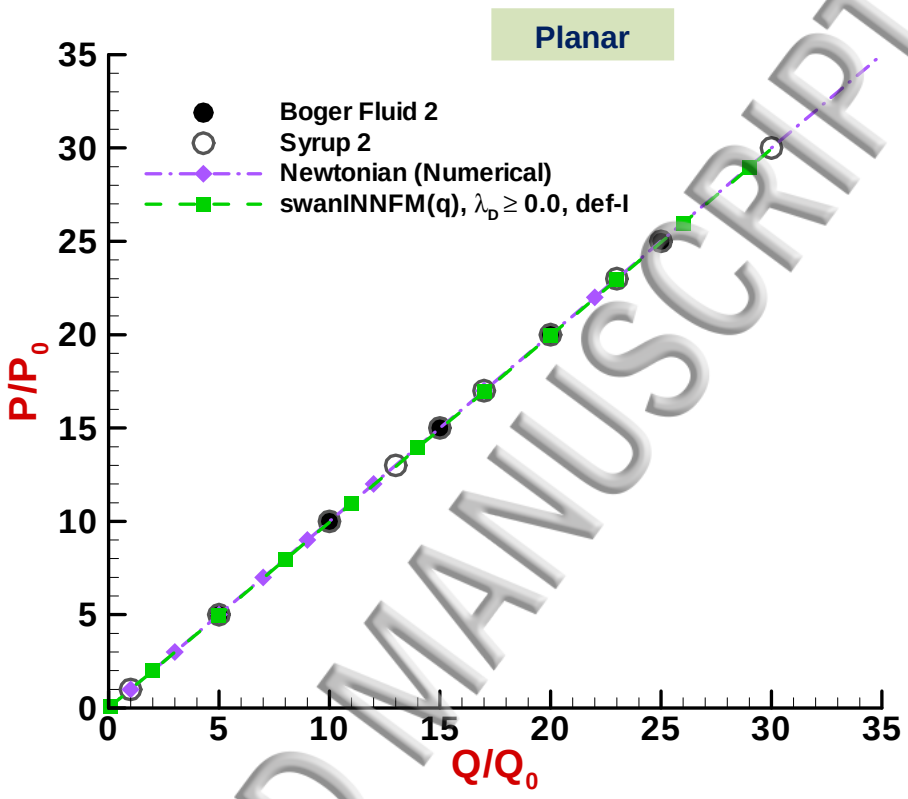

Figure 11. Pressure-drop vs flow-rate, Nigen and Walters (2002) 4:1 experimental vs swanINNFM(q) models, *planar contraction*

6.*2 Planar case*

Considering the counterpart predictive matching for the 4:1 planar contraction problem and the same two fluids, Newtonian and Boger Fluid 2, one may refer to Figure 11. Here, there is a null response between these two fluids in the trends of departure of pressure-drop with rising flow-rate. This is replicated in both the experimental ΔP-data and the predictions with the swanINNFM(q) model. Note, that under planar conditions, through the conventional definition adopted of the generalised strain-rate (definition-I), the extensional viscosity model (swanINNFM(q)) collapses to the base FENE-CR form (with $\lambda_D \geq 0.0$ and $\dot{\varepsilon}=0$, so that $\phi(\dot{\varepsilon})=1$; see above).

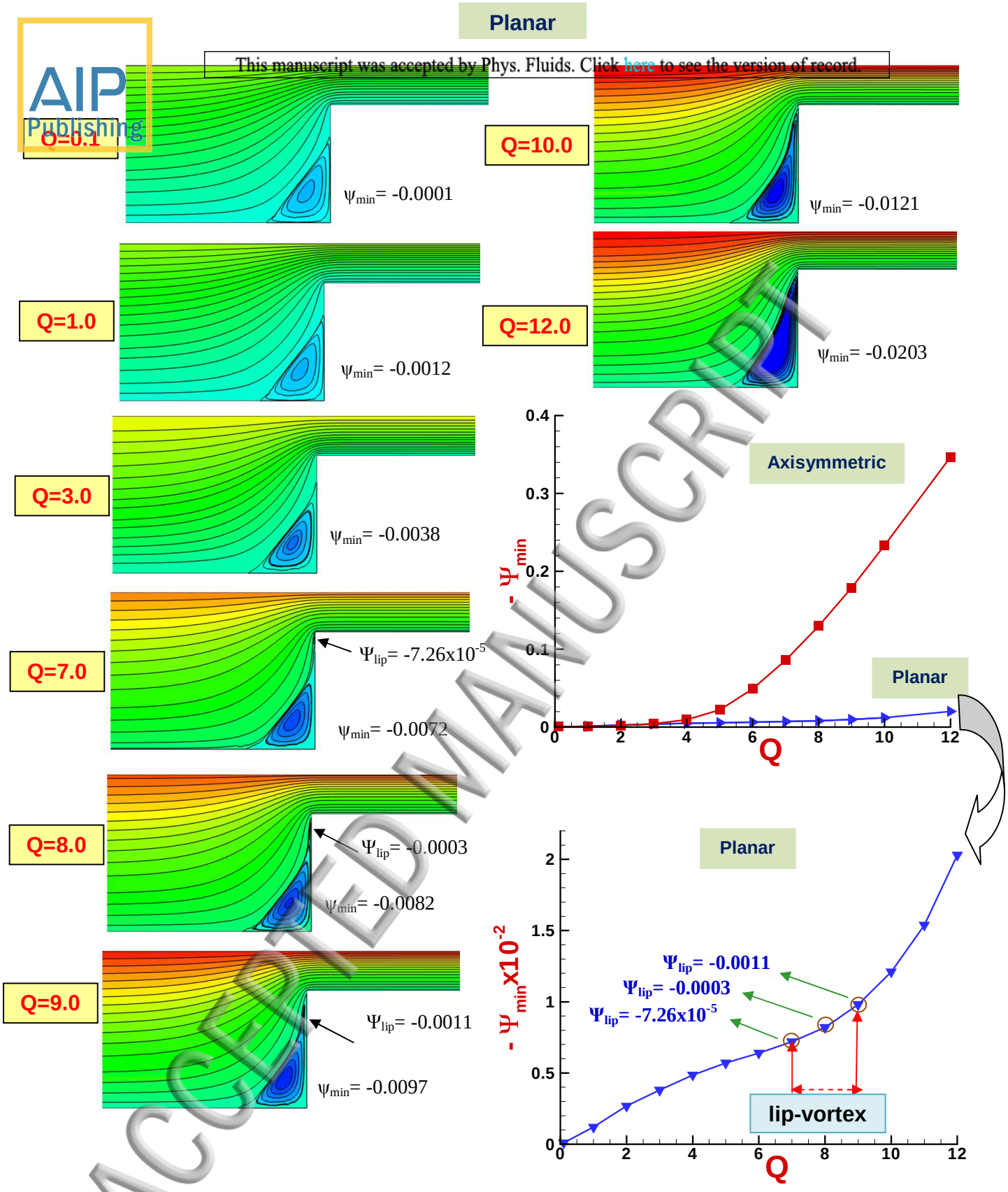

Figure 12A. Streamlines and salient-corner vortex intensity (ψ_{min}, planar vs axisymmetric) at various flow-rates ($0.1 \leq Q \leq 12$), swanINNFM(q) model, 4:1 *planar contraction*

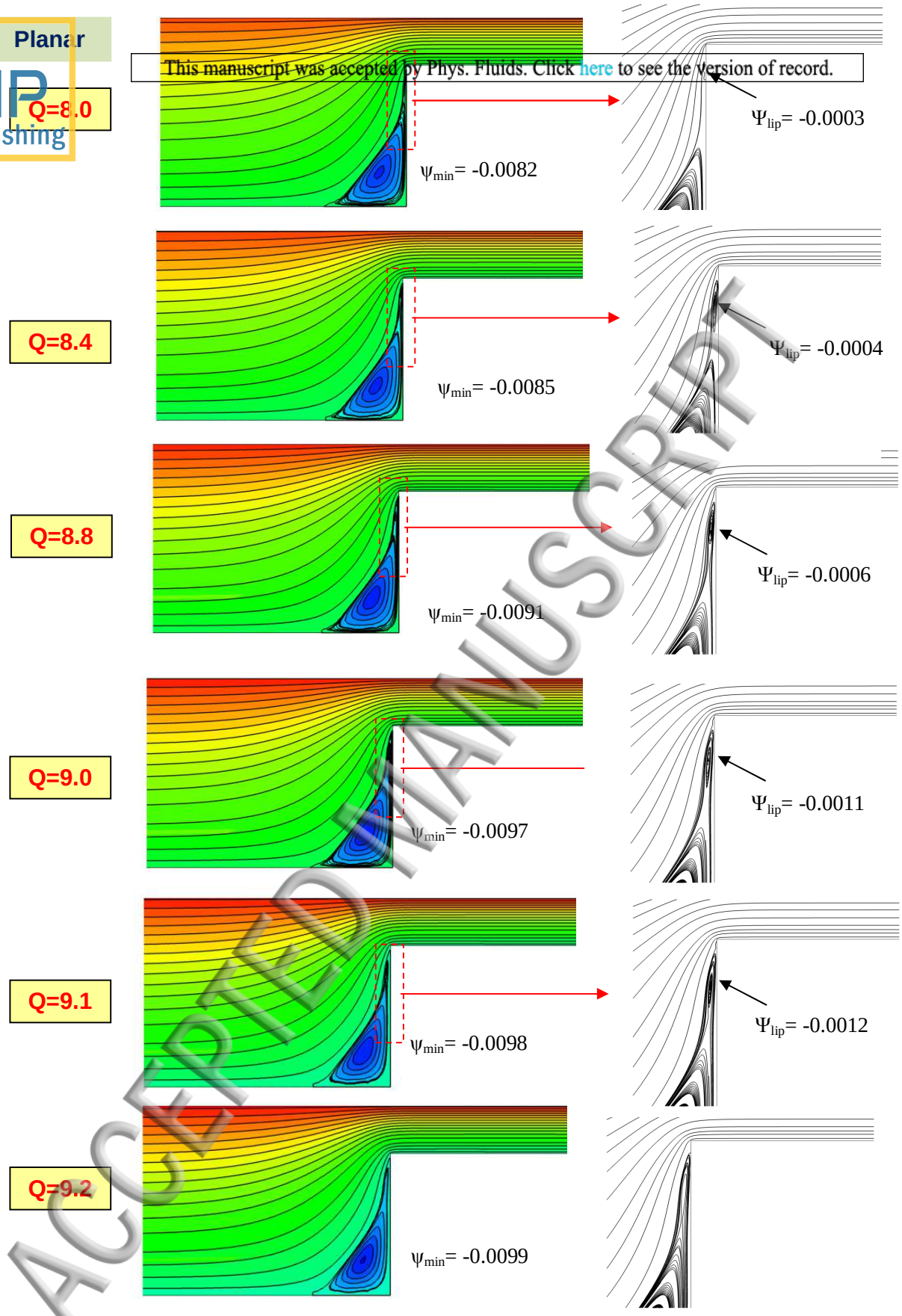

Figure 12B. Streamlines at various flow-rates (8.0≤Q≤9.2), swanINNFM(q) model, λ_D=0.0, *planar contraction*

Figure 12A displays the associated position of planar vortex trend with flow-rate (Q) rise from ~0.1 to ~12 units. The principal salient-corner vortex rises in its intensity from 10^{-4} to $2.03*10^{-2}$. Upstream vortex lengths change negligibly, whilst the vortex gradually grows to cover the front-face of the contraction-plane (towards the sharp re-entrant corner); such coverage is completed between Q=3 and Q=7 units. The upper trend graph in Figure 12A, conveys the planar salient-corner vortex-intensity trend, shown in contrast to that for the counterpart circular case. Clearly, the circular case vortex enhancement is extremely large in comparison. At Q=7 units, a miniscule lip-vortex is also detectable of intensity ($7.26*\ 10^{-5}$), compressed tightly within the cap-zone approaching the re-entrant corner. The intensity of this lip-vortex then significantly magnifies up to ($1.1*\ 10^{-3}$) by Q=9 units. An additional zoomed lower-graph is provided in Figure 12A, for the planar salient-corner vortex-intensity alone, showing the narrow range of flow-rates in which the lip-vortex appears. In Figure 12B**,** the growth characteristics of the lip-vortex are tracked between Q=8 and Q=9.1 units. This trend is accompanied by an increasing salient-corner vortex**.** Then, between Q=9.1 and Q=9.2 units, the salient and lip-vortices have merged, through fingering of the salient-corner vortex into the re-entrant corner region, so that only a single vortex structure survives.

One notes that the planar flow vortex structure is distinctly different when compared to its circular counterpart. Clearly, planar salient-corner vortex-intensity is much smaller than that observed in axisymmetric flows up to Q=12. For example, at λ_D=0.0 and with flow-rate levels of around Q=7 units, planar vortex-intensity (ψ_{min}=-0.0072 units, see Figures 12A) is some ten times smaller than in the circular case (ψ_{min}=-0.086 units, see Figures 7A).

Moreover, for the planar contraction, one notes that the pressure-drop data extends out to an expanded range of flow rates up to 30 units, some three times larger than that reported in the circular case (where strong early vortex activity was apparent). In the planar case, only linear trends are detected in the pressure-drop, with no departure between the viscous and viscoelastic fluids. Also, vortex enhancement was not evident up to Q~12 units. For consistency reasons, we have also checked the position on planar vortex activity for the higher flow rates beyond Q=12 units up to Q=30 units. This has revealed the surprising outcome that in this extended range, indeed beyond Q=15 units, an alternative and later growth trend is predicted in which vortex-enhancement (mainly intensity) now becomes apparent (see Figure 13, slope of line for vortex growth of ~3 for the circular configuration and ~8/9 slope for the planar case). For example, vortex intensity at Q=30 units (ψ_{min}=-0.318 units) is some six times larger than at Q=15 units (ψ_{min}=-0.0493 units), which itself is some two times larger than at Q=12 units (ψ_{min}=-0.0203 units). Note that correspondingly, the separation line adjusts in shape - from concave to convex,

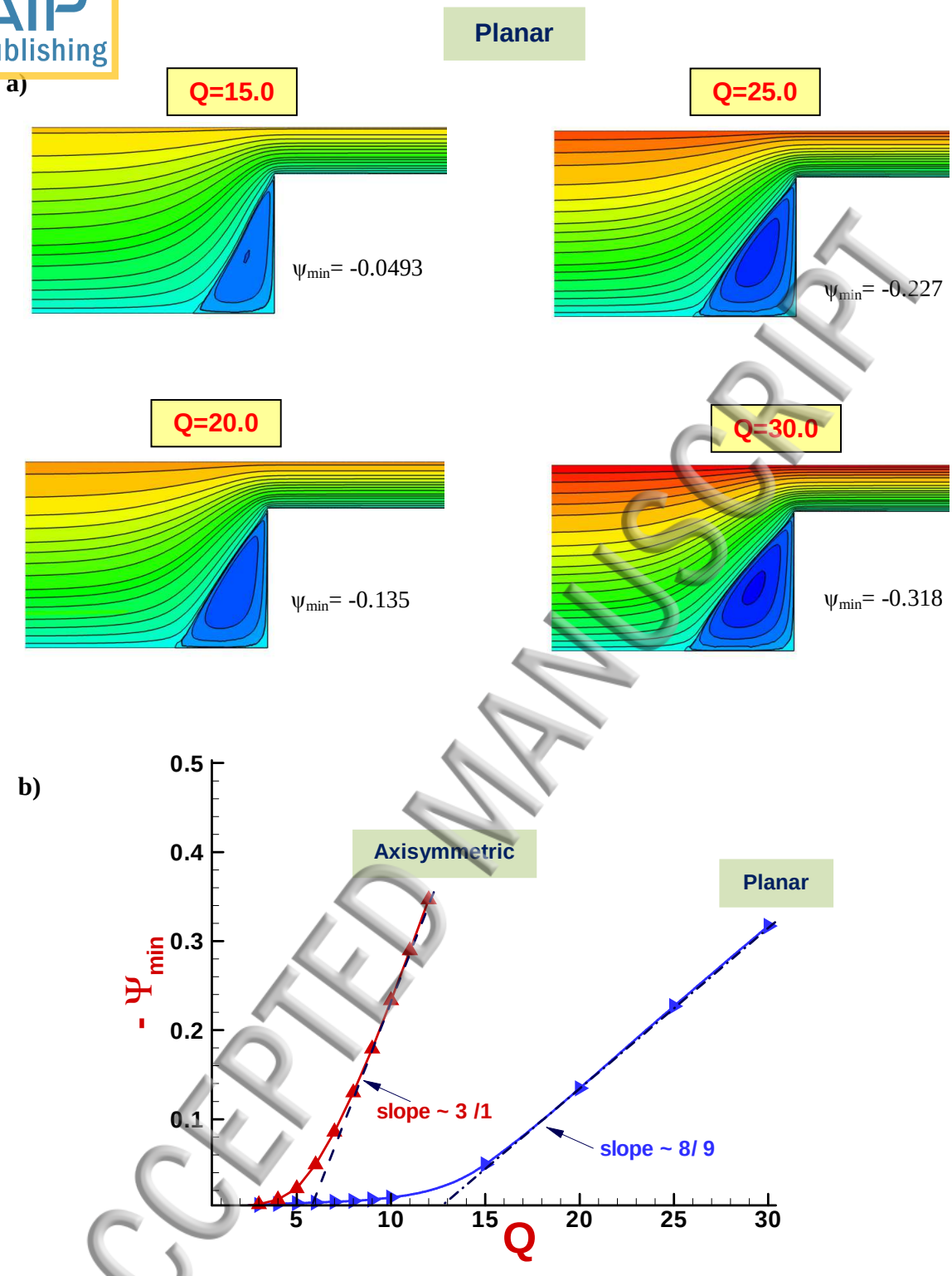

Figure 13. a) Streamlines (*planar contraction*), b) salient corner vortex intensity (ψ_{min}, planar vs axisymmetric); various flow-rates, swanINNFM(q) model

with increasing flow rate from Q = 15 to Q = 30 units and with orientation as perceived taken from the recess corner.

More can be said about the trends in the theoretical vortex activity in the planar-contraction case, but here, we do not wish to detract attention from our basic message and interest in predicting the provocative pressure-drop/flow-rate experiments of Nigen and Walters (2002). (Please see Appendix I for a fuller discussion on the trends in planar-vortex activity).

7. Conclusions

So far as 'flow resistance' is concerned, we are encouraged by the *quantitative* agreement between the present numerical predictions for the swanINNFM model and the experimental data provided by Nigen and Walters (2002). We believe this to be a major step forward in the much sort-for *quantitative* agreement between experimental data and numerical predictions. Notably, one can observe that extremely high pressure-drops may be attained with a suitable selection of the extensional viscous time-scale λ_D .

The particular vortex structure was not a major concern in the Nigen and Walters work, but convincing evidence of early and immediate vortex enhancement for Boger fluids in axisymmetric contractions has been provided. However, there is no such equivalent evidence of strong early vortex enhancement in the planar case.

The numerical solutions we have provided in Figures 6 to 12, for the flow structure in both axisymmetric and planar contractions, are certainly consistent with expectation and the data in Tables 1 and 2.

Acknowledgements

Financial support (scholarship to J.E.L.-A.) from Consejo Nacional de Ciencia y Tecnologia (CONACYT, México) is gratefully acknowledged.

This manuscript was accepted by Phys. Fluids. Click here to see the version of record.

Appendix I

Since, in the planar case, there are no pressure-drop differences from the viscous case to drive such vortex response – one must look elsewhere for stimulation of this delayed *planar* outcome. Hence, one may interrogate stress response, and in particular, localised *extra-stress N_1 and N_2-influences*[2], as displayed through vortex stress-intensity trend graphs, in Figures 14 (planar), 15 (circular). It is clearly apparent that the planar N_1-intensity graph, in the vortex zone (Figure 14(a)), correlates closely with the vortex intensity findings, both in terms of *vortex growth characteristics* and *upturn/onset of enhancement*. In addition, the properties displayed in the *planar* N_2-intensity graph (also, Figure 14(b)) reflect a fairly linear increasing trend (devoid of upturn), only similar to that in N_1-intensity up to Q~10 units. Trends in vortex area-occupation (identified through (L_u) upstream wall length to separation point), follow and agree through streamlines to N_2-intensity (see third graph, Fig.14(c)). Returning to the circular case, to check counterpart states of *localised N_1 and N_2*, in contrast to the planar case, one may consult Figure 15. Now, we see that N_1- and N_2-intensity graphs follow similar trends, illustrating that in the vortex zone, circular-N_1 is almost entirely composed of N_2. Hence, in the circular case, such a trend now tightly reflects the vortex enhancement observed in the streamline intensity, specifically for the flow-rate range Q≤12 units.

[2]For a non-Newtonian elastic liquid, the polymeric stress tensor components τ_{ik} can be written in the form: $N_1 = \tau_{11} - \tau_{22}$, and $N_2 = \tau_{22} - \tau_{33}$. Thus, N_2 is defined in axisymmetric flow as $N_2 = \tau_{22} - \tau_{33} = \tau_{rr} - \tau_{\theta\theta}$, and in planar flow as $N_2 = \tau_{22} = \tau_{yy}$, covering both flow contingencies, as necessary. Then, N_1 and N_2 are the so-called first and second normal stress-differences.

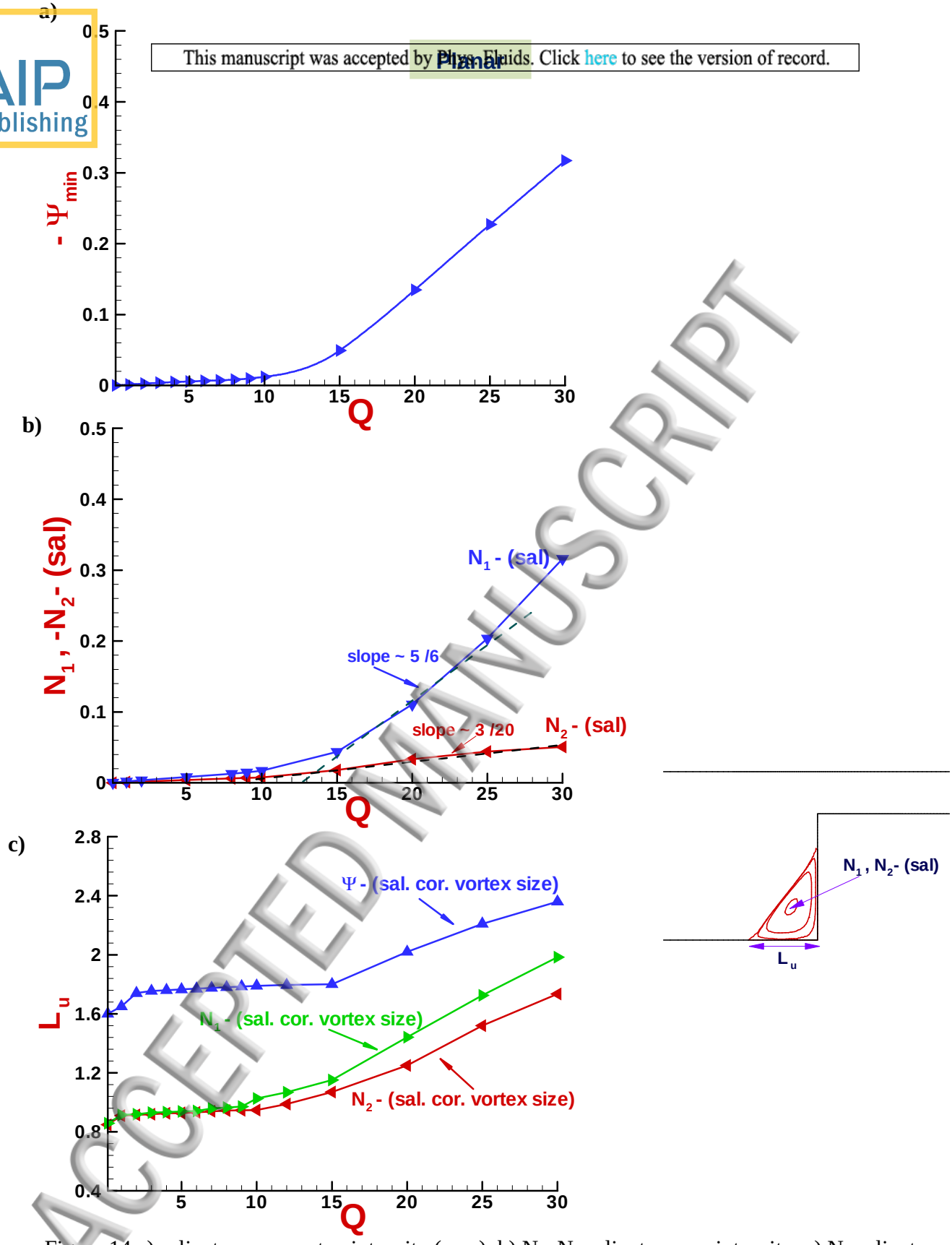

Figure 14 a) salient corner vortex intensity (ψ_{min}), b) N_1, N_2 salient-corner intensity, c) N_2 salient-corner zone-size, swanINNFM(q) model, *planar contraction*

Axisymmetric

a)

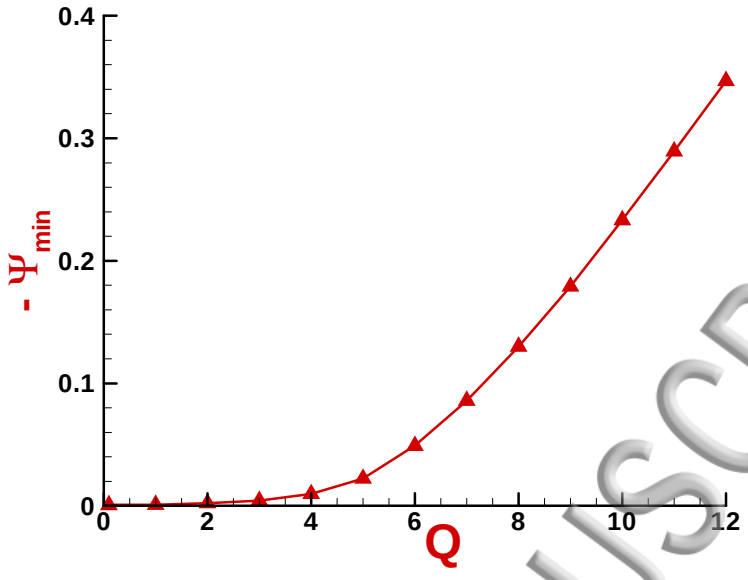

b)

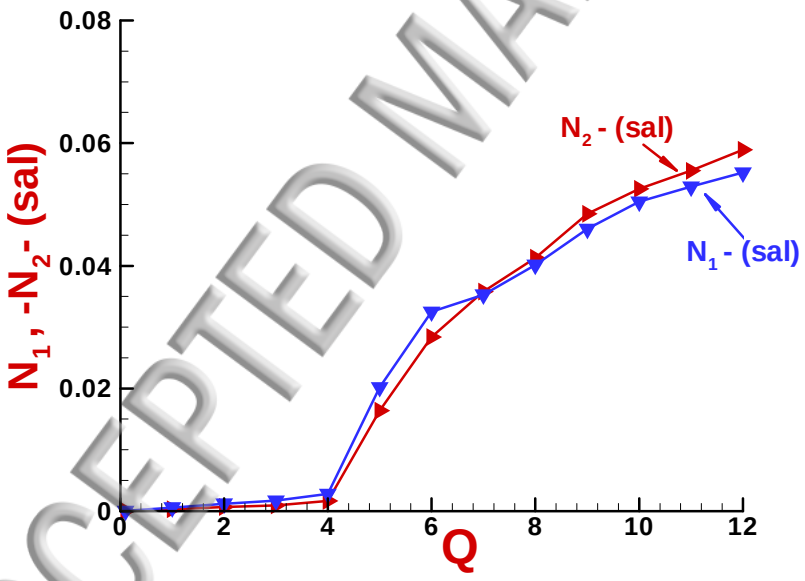

Figure.15 a) salient corner vortex intensity (ψ_{min}), b) N_1, N_2 salient-corner intensity, swanINNFM(q) model , *axisymmetric contraction*

Appendix II:

In the particular instance of the planar deformation, where the conventional definition of generalised rate-of-strain (definition-I) yields a null field value, an alternative definition-II may be proposed, based on the first and second invariants instead, as in: $\Sigma_{gen} = \dot{\varepsilon} = 0.5 trace(|D|)/(1+\sqrt{I_2})$, where again, $I_2 = \frac{1}{2}\det(D^2)$. This version is seen to yield the required form in extension, vanishes in shear and is non-zero yet tractable in complex flow; reflecting similar properties to those of the original, conventional definition in axisymmetric flow. Scaling with $\sqrt{I_2}$, is necessary to render solution tractability around the re-entrant corner. Imposing the absolute operator in the trace function, extracts the extension rate in pure extension. A field plot of the generalised rate-of-strain in planar flow (definition-II), thus generated, is provided in Figure 16 at the elevated flow-rate value of Q=20 units. The corresponding pressure-drop predictions extracted with the swanINNFM(q) model, definition-II strain-rate and dissipative factor of λ_D=1.2 (as in axisymmetric), are displayed in Figure 17. Here, solutions are contrasted against the data provided above, with the experimental measurements for a Boger fluid of Nigen and Walters (2002), and swanINNFM(q) solutions for definition-I strain-rate and dissipative factor of $\lambda_D \geq 0$. In this fashion, the quality of matching to the experimental data is seen to be upheld, as above.

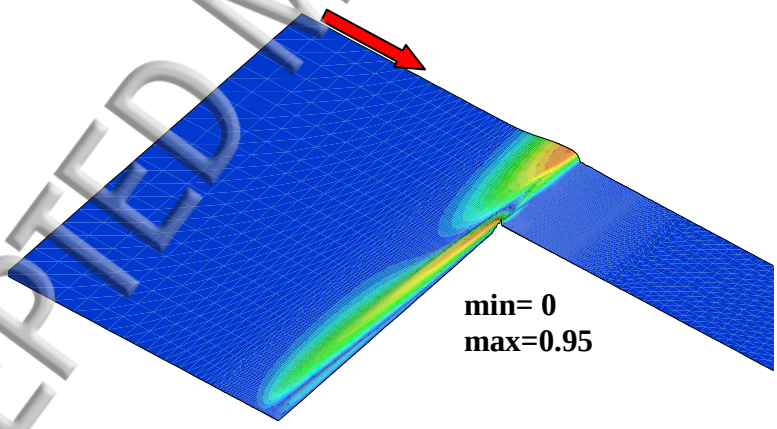

Figure 16. Generalised rate-of-strain in planar flow ($\Sigma_{gen} = \dot{\varepsilon} = 0.5 trace(|D|)/(1+\sqrt{I_2})$), swanINNFM(q) model, Q=20

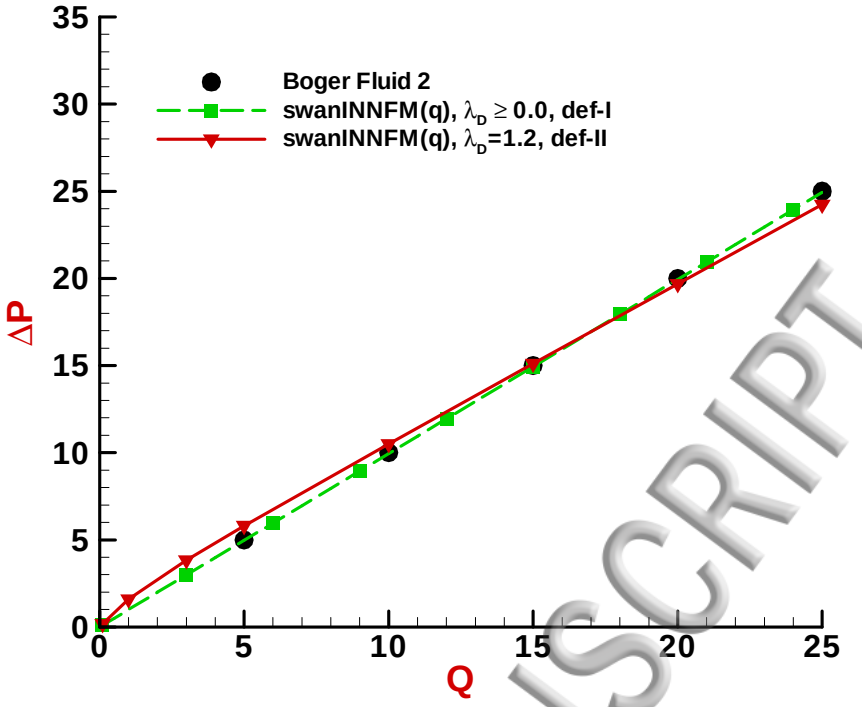

Figure 17. Pressure-drop vs flow-rate, Nigen and Walters (2002) 4:1 experimental vs swanINNFM(q) models, *planar contraction*

References

Abdul Karem T., Binding D.M, Sindelar M; Contraction and expansion flows of non-Newtonian fluids, *Composite Manufacturing*, 4 (2): 109-116 (1993).

Aboubacar M., Matallah H., Tamaddon-Jahromi H.R. and Webster M.F., Numerical prediction of extensional flows in contraction geometries: hybrid finite volume/element method, *J. Newtonian Fluid Mech.* 104: 125-164 (2002).

Aguayo J.P., Tamaddon-Jahromi H.R, and Webster M.F., Excess pressure-drop estimation in contraction and expansion flows for constant shear-viscosity, extension strain-hardening fluids, *J. Newtonian Fluid Mech.* 153: 157–176 (2008).

Alves M.A., Oliveira P.J. and Pinho F.T., Benchmark solutions for the flow of Oldroyd-B and PTT fluids in planar contractions, *J. Non-Newtonian Fluid Mech.* 110: 45-75 (2003).

Alves M.A., Oliveira P.J. and Pinho F.T., On the effect of contraction ratio in viscoelastic flow through abrupt contractions, *J. Non-Newtonian Fluid Mech.* 122: 117-130 (2004).

Baaijens F.P.T., An iterative solver for the DEVSS/DG method with application to smooth and non-smooth flows of the upper convected Maxwell fluid, *J. Non-Newtonian Fluid Mech.*75: 119-138 (1998).

Baloch A., Webster M.F., A Computer Simulation of Complex Flows of Fibre Suspensions; *J. Comput. Fluids*, 24: 135-51 (1995)

Binding D.M., Phillips P.M., and Phillips T.N., Contraction-expansion flows: The pressure drop and related issues, *J. Non-Newtonian Fluid Mech.* 137: 31-38 (2006).

Boger D.V., A highly elastic constant-viscosity fluid, *J. Non-Newtonian Fluid Mech.* 3: 87-91 (1977/1978).

Boger D.V., Hur D.U., and Binnington R.J, Further observations of elastic effects in tubular entry flows, *J. Non-Newtonian Fluid Mech.* 20: 31-49 (1986).

Boger D.V., Walters K., *Rheological Phenomena in Focus*, Elsevier Science Publishers B.V. (1993).

Castillo-Tejas J., Castrejón-González O., Alvarado J.F.J. an Manero O. Prediction of excess pressure drop in contraction–expansion flow by molecular dynamics: Axisymmetric and planar configurations, *J. Non-Newtonian Fluid Mech.*210: 1-11 (2014).

Chilcott M.D., Rallison J.M. Creeping flow of dilute polymer solutions past cylinders and spheres, *J. Non-Newtonian Fluid Mech.* 29: 381-432 (1988).

Cogswell F.N., Measuring the extensional rheology of polymer melts, *Tran. Soc. Rheol.*, 16: 383-403 (1972).

Crochet M.J., Davies A.R. and Walters K. Numerical Simulation of non-Newtonian flow. Elsevier, Amsterdam (1984)

Debbaut B., Crochet M.J. Extensional Effects in Complex Flows, *J. Non-Newtonian Fluid Mech.* 30 (2-3) 169-184 (1988).

Debbaut B., Crochet M.J., Barnes H.A. and Walters K. Extensional effects in inelastic liquids, Xth Inter. Congress on Rheology, Sydney 291-293 (1988).

Garduño I.E., Tamaddon-Jahromi H.R., Walters K. and Webster M.F. The interpretation of a long-standing rheological flow problem using computational rheology and a PTT constitutive model, *J. Non-Newtonian Fluid Mech.* http://dx.doi.org/10.1016/j.jnnfm.2015.12.004 (2016a).

Garduño I.E, Tamaddon-Jahromi H.R. and Webster M.F. The falling sphere problem and capturing enhanced drag with Boger fluids, *J. Non-Newtonian Fluid Mech.* 231: 26–48 (2016b)

Guénette M, Fortin M. A new mixed finite element method for computing viscoelastic flows, *J. Non-Newtonian Fluid Mech.* 60: 27-52 (1995)

López-Aguilar J.E, Webster M.F., Tamaddon-Jahromi H.R., and Manero O. High-Weissenberg predictions for micellar fluids in contraction–expansion flows, *J. Non-Newtonian Fluid Mech.* 222: 190–208, doi:10.1016/j.jnnfm.2014.11.008 (2015).

Matallah H., Townsend P., and Webster M.F. Recovery and stress-splitting schemes for viscoelastic flows, *J. Non-Newtonian Fluid Mech.* 75: 139-166 (1998).

McKinley G.H., Raiford W.P., Brown R.A. and Armstrong R.C. Nonlinear dynamics of viscoelastic flow in axisymmetrical abrupt contractions, *J. Fluid Mech.* 223: 441–456 (1991).

Nigen S., Walters K., Viscoelastic contraction flows: comparison of axisymmetric and planar configurations, *J. Non-Newtonian Fluid Mech.*, 102: 343-359 (2002).

Owens R.G., Phillips T.N., *Computational Rheology*, Imperial College Press, London. (2002).

Pérez-Camacho M., López-Aguilar J.E., Calderas F., Manero O. and Webster M.F. Pressure-drop and kinematics of viscoelastic flow through an axisymmetric contraction–expansion geometry with various contraction-ratios, *J. Non-Newtonian Fluid Mech.*, 222: 260-271 (2015).

Phillips T.N., Williams A.J. Comparison of creeping and inertial flow of an Oldroyd B fluid through planar and axisymmetric contractions, *J. Non-Newtonian Fluid Mech.* 108: 25-47 (2002).

Rallison J.M. Dissipative stresses in dilute polymer solutions, *J. Non-Newtonian Fluid Mech.*, 68: 61-83 (1997).

Rothstein J.P., McKinley G.H. Extensional Flow of a Polystyrene Boger Fluid through a 4:1:4 Axisymmetric Contraction-Expansion, *J. Non-Newtonian Fluid Mech.* 86 (1-2) 61-88 (1999).

Rothstein J.P., McKinley G.H. The axisymmetric contraction-expansion: the role of extensional rheology on vortex growth dynamics and the enhanced pressure drop, *J. Non-Newtonian Fluid Mech.* 98: 33-63 (2001).

Tamaddon-Jahromi H.R., Webster M.F. and Williams P.R., Excess pressure drop and drag calculations for strain-hardening fluids with mild shear-thinning: Contraction and falling sphere problems, *J. Non-Newtonian Fluid Mech.* 166 939–950, doi:10.1016/j.jnnfm.2011.04.009 (2011).

Tamaddon-Jahromi H.R., Garduño I.E., López-Aguilar J.E. and M.F. Webster Predicting Excess pressure drop (*epd*) for Boger fluids in expansion-contraction flow, *J. Non-Newtonian Fluid Mech.* 230: 43–67 (2016).

Tanner R.I. Engineering Rheology, 2nd ed., Oxford (2000).

Walters K. A Rheological "Ocean of Truth" *Proc. SASOR*, 13-22 (2006).

Walters K., Webster M.F. The distinctive CFD challenges of computational rheology, *Inter. J. for Numer. Meth. in Fluids*, 43: 577-596 2003).

Walters K., Rawlinson, D.M. On some contraction flows for Boger fluids. *Rheologica Acta* 21: 547-552 (1982).

Walters K., Tanner R.I. The motion of a sphere through an elastic fluid, *in R.P. Chhabra and D. De Kee (Eds.), Transport processes in Bubbles, Drops and Particles* 73-86 (1992)

Walters K., Webster M.F. and Tamaddon-Jahromi H.R Experimental and Computational aspects of some contraction flows of highly elastic liquids and their impact on the relevance of the Couette correction in extensional Rheology, Proc. 2nd Southern African Conference on Rheology (SASOR 2), 1-6 (2008).

Walters K., Webster M.F., and Tamaddon-Jahromi H.R. The White-Metzner model Then and Now, Proceedings of the 25th Annual Meeting of the PPS meeting, Goa, India, IL 02 1–14 (2009a).

Walters K., Webster M.F. and Tamaddon-Jahromi H.R. The numerical simulation of some contraction flows of highly elastic liquids and their impact on the relevance of the Couette correction in extensional rheology, *Chem Eng Sci.* 64, 4632 – 4639 (2009b)

Wapperom P., Webster M.F. A second-order hybrid finite-element/volume method for viscoelastic flows, *J. Non-Newtonian Fluid Mech.* 79 405-431 (1998).

Webster M.F., Tamaddon-Jahromi H.R. and Aboubacar M. (2005) Time-Dependent Algorithms for Viscoelastic Flow: Finite Element/Volume Schemes, *Numer. Meth. Par. Diff. Equ.* 21: 272-296

White J.L., Metzner A.B. Development of constitutive equations for polymeric melts and solutions, J. Appl. Polym. Sci. 7: 1867-1889 (1963).

Figure captions

Table 1. Experimental observations, (e.g. Nigen and Walters (2002))

Table 2. Numerical predictions (e.g. Binding *et al* 2006, Tamaddon-Jahromi *et al* 2011)

Figure 1 Extensional viscosity for Oldroyd-B, FENE-CR, and swanINNFM(q) models, λ_D=[0.0, 1.2]

Figure 2. Schematic diagrams, flow through 4:1 planar and axisymmetric contractions

Figure 3. Zoomed mesh sections, 4:1 contraction geometry (*elements=2986, nodes=6220, dof=38937, h-min=0.0063*)

Figure 4. Pressure/flow-rate data (scaled), Nigen and Walters (2002), 4:1 *axisymmetric contractio*n

Figure 5. Pressure/flow-rate data (scaled), Nigen and Walters (2002), 4:1 *planar contraction*

Figure 6. Pressure drop (ΔP), swanINNFM(q) model, Q=2.8, 7.2, 12; various λ_D, *axisymmetric contraction*

Figure 7A. Streamlines, swanINNFM(q) model, Q=2.8, 7.2, 12; λ_D=[0.0, 1.2], *axisymmetric contraction*

Figure 7B Salient corner vortex intensity (ψ_{min}), swanINNFM(q) model, Q=2.8, 7.2, 12; various λ_D, *axisymmetric contraction*

Figure 8. Streamlines, salient-corner vortex intensity (ψ_{min}), pressure drop (ΔP), swanINNFM(q) model, Q=12; various λ_D, *axisymmetric contraction*

Figure 9. Pressure-drop vs flow-rate, Nigen and Walters (2002) 4:1 experimental vs swanINNFM(q, λ_D=1.2) model, *axisymmetric* contraction

Figure 10. Pressure-drop vs flow-rate with corresponding streamlines, swanINNFM(q) model; λ_D=1.2, 4:1 *axisymmetric contraction*

Figure 11. Pressure-drop vs flow-rate, Nigen and Walters (2002) 4:1 experimental vs swanINNFM(q) models, *planar contraction*

Figure 12A. Streamlines and salient-corner vortex intensity (ψ_{min}, planar vs axisymmetric) at various flow-rates ($0.1 \le Q \le 12$), swanINNFM(q) model, 4:1 *planar contraction*

Figure 12B. Streamlines at various flow-rates ($8.0 \le Q \le 9.2$), swanINNFM(q) model, λ_D=0.0, *planar contraction*

Figure 13. a) Streamlines (*planar contraction*), b) salient corner vortex intensity (ψ_{min}, planar vs axisymmetric); various flow-rates, swanINNFM(q) model

Figure 14. a) Salient corner vortex intensity (ψ_{min}), b) N_1, N_2 salient-corner intensity, c) N_2 salient-corner zone-size, swanINNFM(q) model, *planar contraction*

Figure.15. a) Salient corner vortex intensity (ψ_{min}), b) N_1, N_2 salient-corner intensity,swanINNFM(q) model , *axisymmetric contraction*

Figure 16. Generalised rate-of-strain in planar flow ($\Sigma_{gen} = \dot{\varepsilon} = 0.5 trace(|D|) / (1+\sqrt{I_2})$), swanINNFM(q) model, Q=20

Figure 17. Pressure-drop vs flow-rate, Nigen and Walters (2002) 4:1 experimental vs swanINNFM(q) models, *planar contraction*